ROBOTICS AND MECHATRONICS

# Generating high frame rate MR images using surrogate signals

G.W. (Gerard) Veenstra

MSc Report

**Committee:**
dr.ir. M. Abayazid
dr. H. Naghibi Beidokhti
dr. B. Sirmaçek
dr.ir. F. van der Heijden
dr.ir. F.F.J. Simonis

September 2019

042RAM2019
Robotics and Mechatronics
EE-Math-CS
University of Twente
P.O. Box 217
7500 AE Enschede
The Netherlands

UNIVERSITY OF TWENTE.

MIRA
BIOMEDICAL TECHNOLOGY AND TECHNICAL MEDICINE

CTIT

# MRI & Ultrasound Sensor Fusion

**Retrospective Gating for Real-Time Synthetic MR Images In- & Outside the Bore**

Gerard Veenstra [s1754718] [1*]

**Abstract**

Currently, retrospective gating allows for interpolating free-breathing Magnetic Resonance Imaging (MRI), but in practice it is only used offline and with the patient lying inside the MRI scanner. This paper continues the work on creating a reconstruction algorithm capable of generating synthetic MR images online both while the patient is in- & outside the scanner. The ability to construct free-breathing real-time MR images will be beneficial in both augmenting medical personal and for the development of robotic tools in the medical field by improving cancer tumor segmentation and tracking. Two retrospective gating approaches capable of constructing such synthetic MR images were implemented for performance assessment: one using full MR images as datapoints, Retrospective Image Gating (RIG); and one using k-space lines, Retrospective K-space Gating (RKG). Input data was acquired by letting five participants perform breathing exercises in the MRI scanner in order to induce specific Respiratory Motion (RM) patterns. At the same time, sagittal MR images of the liver were being acquired at 1.27Hz alongside one-dimensional, ultrasound measurements of the upper right abdomen at 50Hz. The following types of breathing were performed: normal, breath-hold, shallow, deep and coughing. This information enabled the performance assessment of synthetic MRI construction algorithms for different types of RM patterns. The algorithms performed better on the regular, breath-hold and shallow breathing types and considerably worse on the deep and coughing breathing types. An enhancement based on Locally-Sensitive Hashing (LSH) was implemented in order to reduce execution time and make the algorithms closer to real-time. LSH reduced computation time by 20% and 50% on average for RIG and RKG respectively. Post-processing of the MR images was also implemented and evaluated. Post-processing of the generated images produced significantly better results overall. Both algorithms perform better as more data is loaded in for training and thereby produce smoother motion of the liver in the generated video. RKG produced smoother liver motion for the regular breathing type than RIG indicating a better approximation of the real motion; RIG requires more training data to reach the same smoothness. RKG also has a higher perceived image quality as measured by with the Perception-based Image Quality Evaluator (PIQE) metric.

**Keywords**

Medical Robotics — Respiratory Motion Estimation (RME) — Sensor Fusion — Surrogate Signals — Magnetic Resonance Imaging (MRI) — Ultrasound (US) — Learning Algorithms

[1] *Department of Robotics and Mechatronics (RaM): Medical Robotics Group, University of Twente, Enschede, The Netherlands*
***Corresponding author**: g.w.veenstra@student.utwente.nl

## Contents

**1 Introduction** 2
1.1 Background 2
1.2 Objective 4
**2 Related Work** 4
**3 Problem Statement** 5
3.1 Current Situation 5
3.2 Future Situation 5
3.3 Challenges 6
3.4 Research Questions 6
**4 Methodology** 6
4.1 Synthetic MRI Approaches 6
4.2 Data Acquisition 7
4.3 Performance Metrics 9
4.4 Pre- & Post-Processing 11
4.5 Enhancements 12
4.6 Experiments 12
**5 Results & Discussion** 13
5.1 Data Acquisition 13
5.2 Pre- & Post-Processing 14
5.3 Enhancements 15
5.4 Performance Per Activity 15
5.5 RIG Versus RKG 16
**6 Limitations** 16
**7 Conclusions** 17
**Acknowledgments** 18
**Appendices** 20
A Pulser/Receiver House Of Quality 20
B RIG with De-hazing Results 21
C RKG with De-hazing Results 25
D RIG Versus RKG 29

# 1. Introduction

Magnetic Resonance Imaging (MRI) is of high interest as an imaging modality for surgical operations (e.g. biopsy, ablation, etc.) due to its non-invasiveness, high resolution and contrast; in particular, when needles and probes are used to treat small low-volume targets in the liver such as early-stage cancer tumors [1]. MRI is not only used to diagnose a patient before and after surgery, but it is also used as an intra-operative imaging modality to assist medical personnel during surgery. The non-invasive characteristics of MRI is especially important for this application, but it also provides more detail on soft tissues than Computed Tomography (CT) and Ultrasound (US).

One type of surgical procedures which can utilize the advantages of MRI is Minimally Invasive Surgery (MIS). MIS techniques are used to diagnose and treat diseases locally. An applicator such as a needle or probe is used to: sample tissue, deliver drugs or apply treatment (e.g. ablation).

Worldwide 8.2% of cancer caused deaths are caused by liver cancer in 2018 [2]. MIS techniques have become common practice when working with focal hepatic lesions due to the following advantages: less scarring, shorter hospital stays,lower significant-complication rates and lower cost [1]. The technical term ”focal hepatic lesions” refers to low volume lesions/tumors in the liver. These MIS procedures require a high degree of accuracy for which real-time guidance modalities, like ultrasound, are used. Although accuracy requirements are situationally dependant, generally an error of up to two millimeter is regarded as satisfactory. However, these modalities depend significantly on the skill and coordination off the operator [3]. Therefore these operations could benefit from (partial) automation.

Robotic tools will require constant information about the patient with minimal delay and MRI has a relatively long acquisition time. An acquisition time of several seconds is not uncommon for a 2D image, although this is highly dependant on the chosen settings. Much research has been conducted on speeding up the this process. Another core issue with MRI are Respiratory Motion (RM) artifacts, similar to motion blur in photography. RM is the technical term for breathing motion. Therefore patients who breath freely during a scan create RM artifacts in MR images which are problematic for clinical diagnostics. A solution to this problem is to make the patient hold their breath, however not every patient is able or willing to do so.

Therefore the aim should be to create the ability of constructing free-breathing real-time MRI. This will be beneficial in augmenting medical personal and for robotic tools in the future by reducing the demands on patients and improving surgery automation through better tumor targeting and tracking. Currently, there is one prevalent technique to create free-breathing MRI in the medical field: retrospective gating. This enables the reconstruction of synthetic, or artificially created, MR images by using a surrogate signal which is acquired at a higher speed than the MR images. Common surrogates are respiratory belts and navigator echo's, while Inertial Measurement Unit (IMU) and ultrasound surrogates are being under development.

The following sections will explain these concepts and provide the necessary background.

## 1.1 Background

### 1.1.1 Magnetic Resonance Imaging (MRI)

Magnetic Resonance Imaging (MRI) exploits the Nuclear Magnetic Resonance (NMR) phenomenon to localize and distinguish tissues in the x, y and z dimensions as described in Table 1. Localization is done using magnetic field gradients and radio pulses at the resonance frequency of protons at a certain magnetic field strength. This frequency is calculated with the Larmor frequency equation: $\omega = -\gamma B$, where $\gamma$ and B stand for the gyromagnetic ratio and magnetic field strength respectively. Resonance is used to only excite a slice of protons in the z dimensions by which the protons in the slice will precess causing a measurable magnetization. Then, a burst of magnetic gradient is used to cause a phase shift along the y-axis, this is called the phase encoding gradient. After which a continuous magnetic field is used as a frequency encoding gradient to cause a change of frequency along the x-axis. The signals received by the MRI receiver coils are parts of the frequency domain representations of the final image, this is due to the frequency encoding step. A specific part of the frequency domain can be sampled by tuning the scanner to a specific phase. This frequency domain is referred to as the k-space in the medical field and the whole k-space is sampled by tuning the scanner to all phase encodings step-by-step. An MR image is formed by performing an Inverse (Fast) Fourier Transform (IFFT) on the k-space a seen in figure 1 after which the magnitude component is commonly calculated for medical diagnosis. The k-space of an MRI is conjugate symmetric and hence theoretically only half of the k-space needs to be sampled to form an MR image [4], however in practice usually at least 70% of the k-space is required and this does reduce the Signal to Noise Ratio (SNR). Each pixel in the MR image is a volume of tissue and is referred to as a voxel.

**Table 1.** Anatomical-axes and -planes and terminology

| Axis: | Direction: | Technical term: |
|---|---|---|
| X | Left-to-Right (LR) | Dextro-Sinister |
| | Centre-to-Sides | Medial-Lateral |
| Y | Front-to-Back | Anterior-Posterior (AP) |
| Z | Head-to-Toe | Superior-Inferior (SI) |

| Plane: | Axes: |
|---|---|
| Sagittal | Y-Z |
| Transverse | X-Z |
| Coronal | X-Y |

The earlier explanation was a textbook description of how an MR image is formed, however various changes and extensions have been introduced over the years to improve MR imaging. Different sequences can be used to measure different physical properties and different acquisition tech-

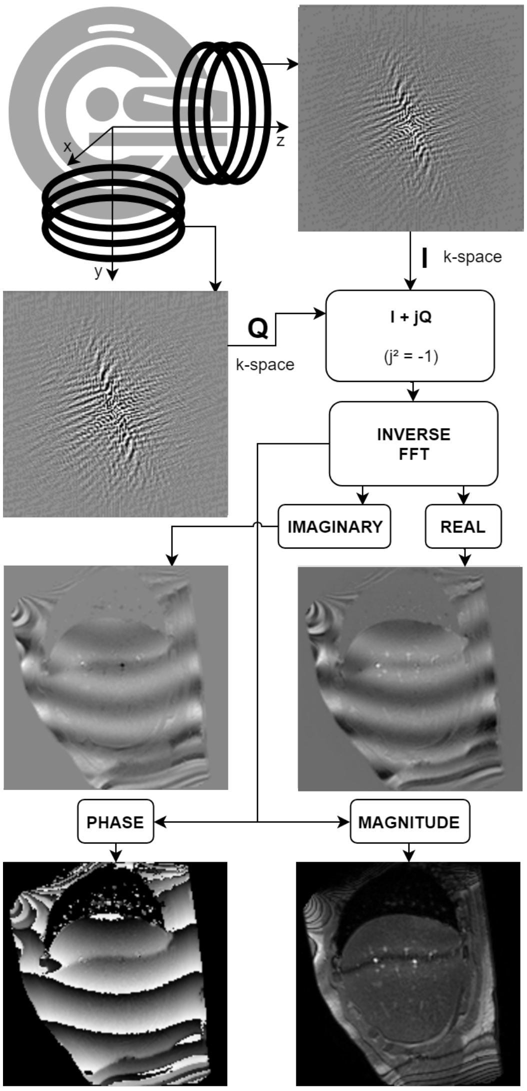


**Figure 1.** Quadrature MRI k-space processing (I: in-phase, Q: Quadrature)

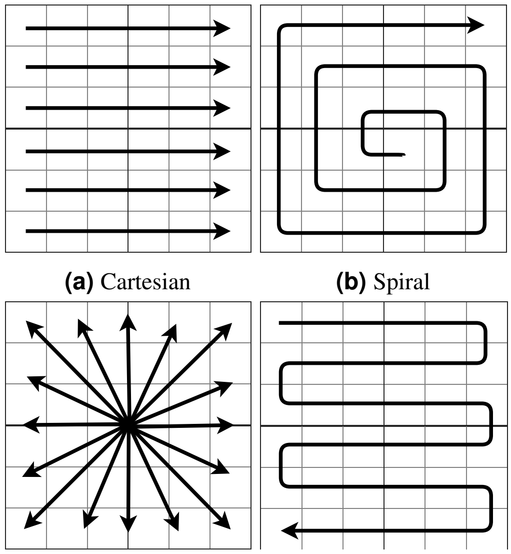

**(a)** Cartesian **(b)** Spiral **(c)** Radial **(d)** Echo Planar Imaging

**Figure 2.** Different types of MRI k-space acquisition trajectories

niques are used to, among others, reduce motion artifacts and change acquisition speed.

The steps of the sequence can be re-timed to measure different physical properties. The time between radio pulses is called the repetition time (Tr) and the time between excitation and measuring is called the echo time (Te). These can be adapted to make a T1 Weighted Image (T1WI), T2 Weighted Image (T2WI) or Proton Density (PD) image. T1 and T2 are properties of protons and depend on the surrounding environment/tissue. T1 and T2 are named longitudinal and transverse relaxation time respectively. A T1WI is characterized by a short Tr and Te and accentuates the T1 properties of the tissues. A T2WI is characterizes by a long Tr and Te and accentuates the T2 properties of the tissues. Finally, a PD image is characterized by a long Tr and short Te and is used to get an indication on the proton density.

Another modification that can be made to formation of an MRI is the acquisition trajectory of the k-space, several types are displayed in Figure 2. The trajectory determines in which way the k-space lines are acquired and in how many cycles an image can be formed. For example, the spiral trajectory in Figure 2b uses one measurement cycle compared to the 6 cycles in the cartesian mode seen in Figure 2a, hence it is faster. However, the spiral trajectory is more prone to motion artifacts than the cartesian trajectory and radial is even less prone to these artifacts [4].

This research focuses on the liver area and hence some important MRI settings for liver imaging have been searched. ”With the current state of the art technology, magnets of 1.5 tesla (T) and 3T field strength are considered the standard of reference in providing high-quality and consistent MR images” [5]. A volumetric resolution of two millimeter or less in each direction with a temporal resolution of three seconds or less is desirable [6]. Diffusion Weighted Imaging (DWI) is a ”highly sensitive modality for [the] detection of focal hepatic lesions” [7].

### 1.1.2 RM Compensation Techniques

There are several techniques used to generate MR images to compensate for motion. One of these techniques is called gating of which there are two types: prospective and retrospective. Prospective gating techniques use a surrogate sensor to start an MRI acquisition when the area of interest is in a particular state. For example, a respiratory belt or bellow is used to measure at which phase of the respiratory cycle a patient is. Prospective gating increases imaging time significantly and in some cases requires the patient to perform a specific breathing instruction. This type of gating is known as a form of triggering. However retrospective gating does not start acquisition at a trigger. For example, an electrocardiogram (ECG) signal is recorded while continuously imaging the heart with an MRI. The acquired k-space lines are then grouped per ECG state and a synthetic MR image is then generated by filling the k-space with the k-space lines of one state.

Many types of surrogate signals exist for gating of which many are hardware-based like the respiratory belt/bellow, ECG and ultrasound. Using navigator echos is another way gating can be performed, these are measurement of a small area made by the MRI itself. They can be acquired fast and therefore support the gating approach.

Other techniques to reduce RM artifacts include pulse sequences which specifically compensate for RM. They oversample the center of k-space, where the most information is stored, essentially using it as a surrogate.

This research will focus on using ultrasound as a surrogate, hence the following section will provide additional background for this surrogate.

#### 1.1.3 Medical Ultrasound Imaging

Medical ultrasound (US) imaging uses sound waves to create an image of the tissue underneath the skin, these images are also known as sonograms. Sonograms are created by recording the reflections/echo of sound waves with a frequency above 20 kHz which are pulsed into the body. Different tissues have different reflection properties which are displayed in the image. A well known use-case of US imaging is the practice of imaging an unborn baby in the womb, obstetric ultrasonography.

The sound wave created by a transducer is aimed with a lens or through the use of beamforming. A method for directing sound by using multiple sources producing sound at different phases and/or magnitudes. Beam-forming/-steering is also used to produce 2D images with a 1D sensor by sweeping the sensor. The measured acoustic reflections are caused by changes in acoustic impedance at the border between two regions, this border is also known as the interface. The intensity and direction of the reflections depend on the difference in material properties at the interface. Commonly, the intensity of the reflection is displayed on a sonogram. Common frequencies used for medical imaging lie between 1 and 18 MHz; Lower frequencies penetrate deeper, but higher frequencies have shorter/smaller wavelength and hence reveal more details. The speed of sound is assumed to be 1540 m/s overall, causing a loss of resolution due to the fact that this assumption does not hold in the different tissues/environments. Another source of noise are reverberations, which can be described as reflections of reflections.

Different modes of medical US imaging exist:

- **A-mode**: is a 1D US sensor showing the reflections on a line through the body.
- **B-mode**: is a 2D US sensor showing the reflections on a plane through the body.
- **C-mode**: is a 2D US sensor showing the reflections on a plane normal to the plane of a B-mode image. A plane at a fixed depth is chosen and the sensor needs to be moved to scan the plane.
- **M-mode**: is a A-/B-mode image taken in rapid succession creating a video.
- **Doppler mode**: makes use of the doppler effect to measure speed of the blood for example.
- **Pulse inversion mode**: uses two pulses with an opposite sign to show contrast between materials and gasses with linear and non-linear compression properties.
- **Harmonic mode**: uses sound at the fundamental frequency of the body after which harmonic overtones are measured. This reduces noise and artifacts due to reverberations and aberration.

### 1.2 Objective

The aim of this research was to continue the work on generating real-time MRI for target: tracking, segmentation and visualization. In this case real-time indicates a frame rate of at least 24 frames per second (FPS) and low latency to allow for a smooth and direct visualization of the body. This would allow surgeons and robotic tools to have access to the MRI modality in- and outside the MRI bore. Inside the bore MR images can be interpolated and outside the bore MR images can be extrapolated from the learned data with the surrogates.

## 2. Related Work

**Giger *et al.* (2018)** introduced the use of 2D US surrogates for MRI-surrogate sensor fusion in the abdominal and compares it to a navigator (slice) based approach [8]. The algorithm selects the MR slice of which the surrogate signal is most similar to the new surrogate signal. Notably two different similarity metrics were used to compare surrogate signals: an intensity based metric and one comparing the position of fudicial points in the US image.

**Berijanian (2018)** focused on finding correlations between surrogate signals and the respiratory motion of a hepatic/liver tumors. Two surrogate signals were used: visual trackers with a camera and an IMU on a needle inserted into the liver. Linear regressions methods were used to predict tumor motion. No conclusion was made about which surrogate signal was better however a combination of the two lead to better estimation results. However only the raw IMU output was used, no attempt was made to integrate the signals in order to calculate a position or displacement. A finite-element Model (FEM) was created to generate repeatable data. The FEM data was used to augment the real measurements. This caused little change in performance from which was concluded that the FEM is a good representation of the real life scenario.

**Fahmi *et al.* (2018)** used visual markers with regression techniques (multivariate, ridge and lasso) to create a Respiratory Motion Estimation (RME) model. This modelled how a target in the liver moved in the body. Lasso seemed to be the better regression technique with a Mean Absolute Error (MAE) below 2mm. "However, the spatial resolution of the acquired MRI liver images prevented a more detailed evaluation of the 3 models"[10], referring to a temporal resolution of 1 second and spatial resolution of 1.5 by 1.5 in the sagittal plane with a slice thickness of 15mm.

**Abayazid *et al.* (2018)** estimated RM with a second reference needle as a surrogate alongside the operative needle [11]. The reference needle included an IMU at its base to measure motion. A correspondence model was created to link the surrogate signal to target displacement. RAkELd, a variant on Random k-Labelset (RAkEL) was used to generate the model from experimental data produced using a gelatin based liver phantom that moved in the anterior-posterior and inferior-superior directions. The estimated target displacement had a mean error between 0.86 and 1.29mm. This approach using a reference needle was sensitive to needle bending, distorting the correlation found by the correspondence model.

**Preiswerk *et al.* (2017)** introduced a method for interpolating frames between MR images using a surrogate ultrasound signal [12]. This allowed for higher framerates and out-of-bore MR images to be formed synthetically.

This approach is a form of online retrospective image gating. The algorithm learns from the MRI and ultrasound data as it comes in. Complications arise in previously unseen situations like coughing for the first time, but mainly when the ultrasound sensor is displaced. The displacement of the sensor can cause the correlation between the historical data en incoming data to be lost and hence compromises the whole system. Another issue is caused by a historical datapoint encompassing a whole MR image and its corresponding set of ultrasound signals. This MR image has been sampled over a relatively long period of time, around 4 to 5 seconds [13]. This causes a datapoint to include motion artifact acquired over a significant part of the breathing cycle which results in blurred synthetic MR images.

**Shokry (2018)** added an enhancement to the approach introduced by Preiswerk *et al.* [13]. It adapted the original approach to compensate for the low acquisition speed of an MRI compared to the respiratory cycle, four to five seconds or up to a quarter of a respiratory cycle [13].

This approach is a form of online retrospective k-space gating. The algorithm learns from the MRI k-space lines and ultrasound data as it comes in. Again, the algorithm is sensitive to surrogate sensor displacement, which causes the loss of correlation between historical and incoming surrogate data. Another issue is the case of previously unseen situations, a user will not know how good the prediction will be. The research claims to use k-space lines as an input to the algorithm, however the used dataset only includes MR magnitude images and hence an approximation is not possible. Supposedly the frequency domain of the magnitude image is used.

The paper also introduced a machine learning algorithm named the ”Evolving function” to map the closeness of a surrogate signal toward a reference signal to the displacement of a target. This algorithm was applied to a visual surrogate signal using: skin markers, a camera and an EM trackers to detect a target in the MRI. The evolving works by picking a minima or maxima of the surrogate signal as a reference. New surrogate data is compared to the reference and a closeness value between zero and one ([0,1]) is calculated. Then during a training phase the evolving graph gets filled where target displacement is filled in for several closeness values. The values between acquired closeness values are linearly interpolated, creating the evolving function.

The evolving function could be sensitive to new minima and maxima when used as an online algorithm, after which the evolving graph needs to be recalculated.

# 3. Problem Statement

## 3.1 Current Situation

Special ”double doughnut” MRI bores have been developed to allow surgeons to effectively work inside the bore with intra-operative MR images [14] since some surgeries require or benefit from these images. However, the noise coming off these bores was too loud for the surgeons to communicate and hence this technique has fallen out of favour. Another method of supporting intra-operative MRI is by either moving the patient or the MRI bore from and to one another, however this only allows surgeons to get a snapshot of their progress and not a continuous stream of up-to-date images during surgery.

Another issue with MRI is its overall slow update speed. Even though the actual speed is highly dependant on the machine, settings and requirements; MRI machines are not capable of real-time imaging without using specialized techniques due to inherent physical properties. In this case real-time indicates a frame rate of at least 24 FPS and low latency to allow for a smooth and direct visualization of the body.

## 3.2 Future Situation

Current research projects are also working towards robotic tools to substitute or augment the surgeon for some tasks in the future [15] . An example of this is the development of pneumatic needle actuators which can be used inside the MRI with minimal magnetic interference [16]. These actuators require a target to navigate to. However, this target will move due to Respiratory Motion (RM) and target tracking is not possible with MRI alone due to the trade-off between resolution and imaging speed when employing MRI. An MR image of sufficient resolution and contrast takes up to a quarter of the respiratory cycle causing motion artifacts due to RM [13].

Common solutions to minimize RM induced artifacts are breath holding and gating techniques [17] . However, these techniques suffer from reduced imaging speed, increased intervention time and inconsistent organ position between breath holds or gating triggers. Breath holding is also ”inconvenien[t] especially for those who suffer from respiration difficulties” [18]. These limitations made the development of free-breathing MRI important.

Motion robust MRI sequences like 2D magnetization-prepared rapid gradient-echo (MP-RAGE) are also used to counteract motion artifacts, but result in moderate image quality [5]; hence new state-of-the-art techniques arose which combined the output from the MRI scanner with surrogate signals such as: A- and B-mode ultrasound; reference needles; Inertial Measurement Units (IMU); visual markers; and more [9], [11]–[13], [19]. These techniques would combine the high resolution and contrast of an MR image needed to distinguish the target with the update speed of the surrogate, an approach known as sensor fusion, to do Respiratory Motion Estimation (RME).

These approaches allow the system to temporally interpolate the MR image inside the MRI bore and temporally extrapolate the MR image outside of the bore with the surrogate signal by creating synthetic MR images. Extrapolating MR images outside of the bore would allow for using non MRI-safe equipment while retaining some of the benefits of MRI. The approach by Preiswerk *et al.* [12] and Shokry [13] also allow for free-breathing MRI, see section 2 for more details.

### 3.3 Challenges

The fusion between MRI and surrogates still has some obstacles to overcome. Approaches using ultrasound (US) surrogates are critically susceptible to the displacement of the ultrasound sensor [12], [13], since this will remove the correlation between historical and newly acquired surrogate data. Systems based on reference needles are sensitive to needle bending which distorts the same correlation [11]. It is also not known how these approaches for generating synthetic MR images proposed by Preiswerk *et al.* and Shokry respond to different types of breathing/RM.

Another challenge arises when we take into account that the system will, in the future, be used in conjunction with robotic systems. These systems will have to compensate for RM, however a delay is always present between observation and action and therefore the robotic system would benefit from real-time MRI and optimally a prediction of near-future motion to compensate for this motion in real-time.

Another issue arises when looking at the work of Shokry [13], the proposed method is based on textbook Cartesian MRI formation. However, this is not identical to currently prevalent and state-of-the-art MRI formation according to specialists. This work also contains a flaw as the data used in this research does not contain phase images and hence would not allow a reconstruction of the k-space, however the algorithm still has potential.

### 3.4 Research Questions

This research focused on evaluating the performance of the synthetic MRI approaches using surrogates under different types of RM. The synthetic k-space approach needed to be validated with real k-space data, as the original work only used the frequency domain of magnitude images. Further contributions focused on enhancing the approaches for better performance.

The following research question was defined:

1. What is the performance of synthetic MR image reconstruction for different types of respiratory motion?
   (a) How can a dataset be created which is suitable for the performance assessment of MRI-ultrasound sensor fusion, respiratory motion classification and prediction?
   (b) Which metrics should be used to asses the performance of synthetic MR image reconstruction?
   (c) How does pre- and post-processing affect performance?
   (d) How can synthetic MR image reconstruction be made real-time?

## 4. Methodology

This research consisted of three critical components: data acquisition, algorithm implementation and data analysis. The implementation of these components are discussed in this section.

### 4.1 Synthetic MRI Approaches

#### 4.1.1 Retrospective Image Gating (RIG)

This approach in combination with ultrasound was introduced by Preiswerk *et al.* [12]. The top row of figure 3 visualizes the algorithm presented in this paper. The method compares a sliding window of the surrogate signal to historical data. The historical data consist of complete MR images and their corresponding surrogate signal. Similarity-weights are given to the historical MR images, where higher weights are given to MR images that were acquired in a similar state compared to the current state as measured by the surrogate signal. The historical MR images are then multiplied by their weight and summed together, this summation is then divided by the total sum of the weights resulting in the new synthetic MRI.

The US signals are pre-processed using the Hilbert transform as shown in equation 1.

$$U = log(abs(hilbert(U_{raw}))) \tag{1}$$

The similarity weights (s) are calculated as shown in equation 2 with the current US signal ($U_t$) and historical US signals ($U_T$). $\Sigma$ is a vector describing the variance of the US signal at every depth, $Tr$ is the repetition time of the MRI sequence, $N_x$ is the number of US depths and $N_{Tr}$ is the number of US acquisitions in the sliding window.

$$s(U_t, U_T) = \nu \cdot \exp\left(-\frac{1}{2}(U_t - U_T)^T \Sigma^{-1} (U_t - U_T)\right) \tag{2a}$$

*where*

$$\nu = (\sqrt{(2\pi)^n \|\hat{\Sigma}\|})^{-1} \tag{2b}$$

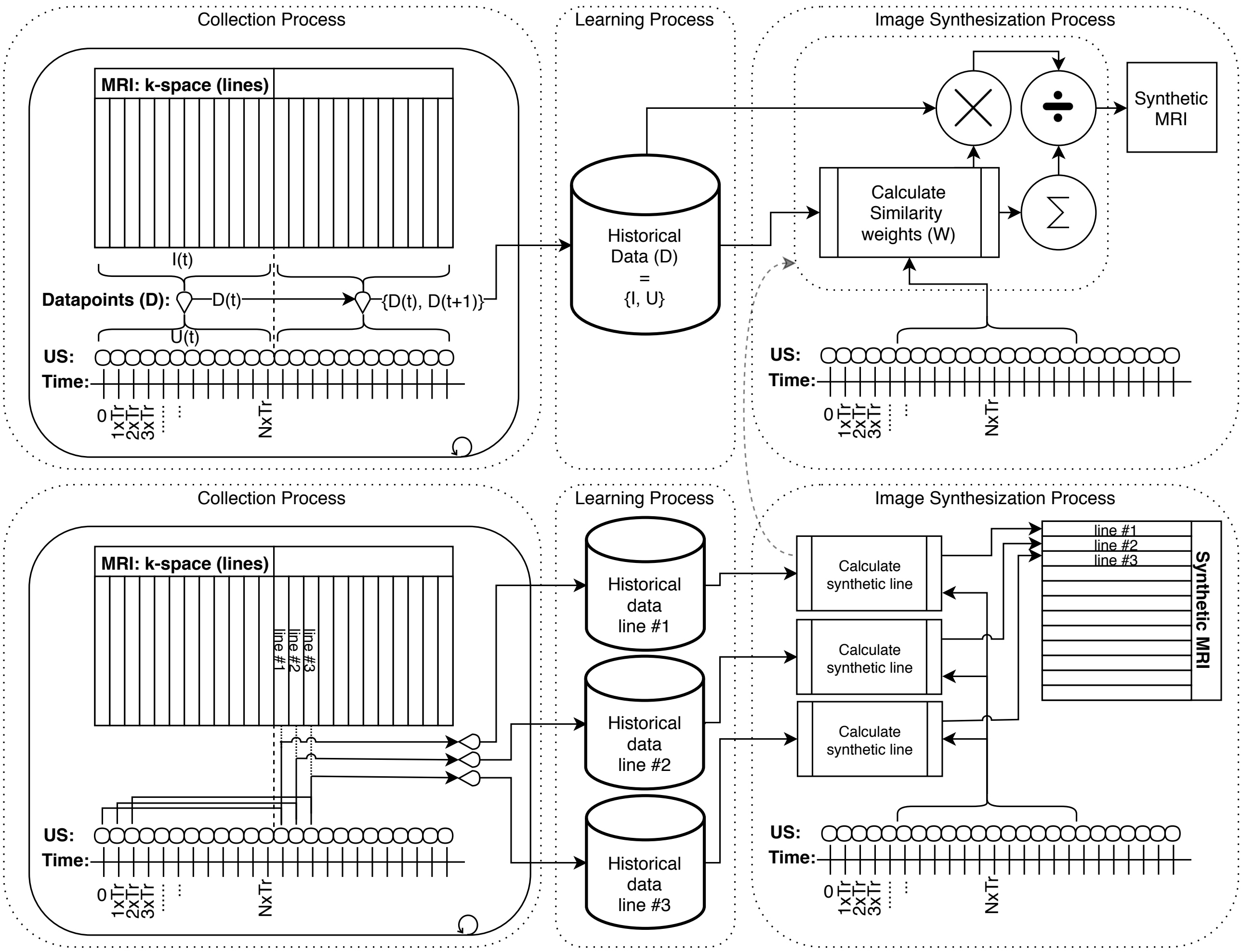


**Figure 3.** Synthetic MRI generation approaches: **top**, Retrospective Image Gating (RIG); **bottom**, Retrospective K-space Gating (RKG)

$$\hat{\Sigma} = \frac{\Sigma}{\exp(\mathrm{Tr}/10) \times \left(\hat{N}_x \times N_{Tr}\right)^2} \tag{2c}$$

#### 4.1.2 Retrospective K-space Gating (RKG)

This approach in combination with ultrasound was introduced by Shokry [13]. The bottom row of figure 3 visualizes the algorithms for synthetic MRI presented in this paper. It is similar to the approach by Preiswerk *et al.*, however a datapoint is a set of surrogate ultrasound signals with one k-space line of the MR image. This is done as the combination of multiple k-space lines acquired at different phases of the respiratory cycle into one image is a cause of motion artifacts. A single k-space line is acquired relatively fast and therefore suffers little from motion artifacts itself. These datapoints are stored separately by line number. A synthetic image is formed by calculating the similarity weights of the historical data on a per line basis. Each line of the synthetic image is formed by multiplying its corresponding historical lines by their similarity weight, summing them together and then dividing them by the sum total of the weights. Another way to look at this approach is as follows: the surrogate signals are used to detect the phase of the respiratory cycle and historical data is collected for a number of phases. The similarity weights are calculated and used to select historical k-space lines that had a similar phase to the phase measured by a set of newly acquired surrogate signals.

#### 4.1.3 Optimizations & Enhancements

The original implementation of the RIG and RKG algorithms included the following performance optimizations. Only a subset of the US surrogate signals was stored in the datapoints as displayed in figure 3. The $N_x$ number of US depths with the highest variance during the initialization phase were stored. Next to this only the K closest similarity matches were used for synthesizing an MR image. During all experiments $N_x$ was set to 200 and K to 6 as discussed by Preiswerk *et al.* and they were not further optimized [12].

### 4.2 Data Acquisition

Data acquisition shows the procedures which were followed in order to create an MRI and ultrasound dataset with (limited) inter-subject variability (gender, age, length, weight) and variation in breathing/RM. The dataset also includes data from a respiratory bellow.

#### 4.2.1 Surrogate Sensors

The following types of sensors were used: 3.5MHz A-mode ultrasound and respiratory bellow. The ultrasound sensor was mounted with adhesive to the skin at the upper right abdomen near the liver. The respiratory bellow was mounted right bellow the ribs at the highest point during exhalation when lying down. For more information see section 4.2.4.

#### 4.2.2 Breathing Types

The following types of breathing/RM were included in the database: regular, normal calm breathing; breath-holding, intermittent 5 to 10 seconds holds at the end of exhalation; shallow, short in- and exhalations; deep, large in- and exhalations; and coughing, intermittently induced.

The main restriction for choosing breathing types was that they need to be consistently artificially inducible by the participant. Regular breathing was chosen as it is the most common type of breathing. Breath-holding was chosen as it is commonly induced in patients who are being scanned in order to reduce RM during imaging. The breath hold was executed at the end of exhalation as this would reduce RM artifacts [20]. Shallow breathing was chosen as it introduces rapid short motion to the dataset and approximates hyperventilation. Deep breathing was chosen as it introduces a slow but large motion to the dataset. Coughing was chosen as it is a common affliction and causes artifacts in MRI scans, sometimes requiring the restart of an MRI scan. It also introduces rapid large motion to the dataset.

The choice was made to try and keep the breathing patterns as naturally as possible, hence the participant were free in choosing which orifice to use and if to breath through the chest or abdomen (diaphragmatic). It would also have been difficult to monitor and confirm that participants followed those instructions.

#### 4.2.3 Data Collection Procedure

Participants were placed lying inside the bore of the MRI scanner with the surrogate sensors attached. For every experiment, the participants age, length and weight were recorded. After which different types of breathing were performed in the MRI. An instructor standing next to the MRI gave the following instructions to the participant:

- 2 minutes of regular breathing
- 2 minutes of intermittent breath holding
- 30 seconds of regular breathing for recovery
- 2 minutes of short and shallow breathing
- 30 seconds of regular breathing for recovery
- 2 minutes of deep and heavy breathing
- 30 seconds of regular breathing for recovery
- 30 seconds minute of intermittent coughing

Two minute segments were chosen since it would provide at least 50 MR images and at least 10 cycles of the different types of breathing. Intermittent coughing was shortened since it became highly uncomfortable for some people during try-out runs of the protocol. The recovery segments are used to allow a person to relax and get back to a rested state after performing an breathing exercise.

The breathing procedure is performed twice in a row; first with scans made with cartesian scanning pattern, followed by scans made with the radial scanning pattern.

#### 4.2.4 Materials

**Figure 4.** Custom ultrasound transducer

**The ultrasound transducer** was used to pulse sound waves into the body and receive the echo. Custom ultrasound transducers were fabricated for this project by Optel (Optel Ultrasound Technology, Poland, Wrocław). The transducers casings were made out of polyoxymethylene (POM) with a diameter of 7mm and height of 2cm. A 2m coaxial cable with a BNC connector is permanently attached to the side of the probes. The transducers had a center frequency of 3.5 and 7.5MHz. The 3.5MHz probe was used in the experiments as it was found that it gave a better signal during preparatory experiments.

**The transducer support brace** was designed to stick the ultrasound transducer onto a persons skin. Figure 5 shows the design of the brace which was 3D printed from ABS filament. Its use is as follows: the transducer is friction fitted in the center channel; the connector cable is routed through the slit; and the brace its flat bottom is stuck onto the skin with adhesive bandage taped over the outer disc. Due to the friction fit the transducer can be set to slightly protrude out from the bottom, this improved contact with the skin.

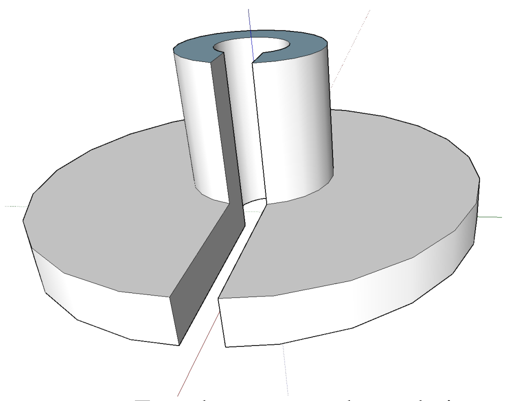

**Figure 5.** Transducer support brace design

**The ultrasound Pulser/Receiver (PR)** is responsible for exciting the piezoelectric crystal in the US transducer after which it measures the return signal. Some PRs are also able to digitize and store the received waveforms while others must use a separate digitizer for this application.

This research used the Optel Opbox V2.1 Mini Ultrasonic Box with Integrated Pulser and Receiver (Optel Ultrasound Technology, Poland, Wrocław) and was selected over other equipment by use of a house of quality as seen in Appendix A. The following requirements were set for the PR with digitizer:

- Portable
- External triggering
- Minimal PRF of 25Hz
- Capable of saving the waveforms continuously at the minimum PRF
- Compatible with the ultrasound transducer

The minimum PRF of 25Hz was set as this would allow synthetic MRI to be generated that would be perceived as a continuous video.

The following settings were used by the Optel Opbox:

- Pulse voltage: 240V (level 10)
- Pulse width: 2.8$\mu$s
- Sampling frequency: 33.3MHz
- Analog filter: 2-6MHz
- Gain: 24 (pre-amplifier) + 15 (constant) dB
- Delay: 10$\mu$s
- (Measurement) Window: 80$\mu$s
- Trigger: timer (PRF)
- PRF: 50Hz

No external triggering was used due to limitations of the MRI, see section 5.1.3.

**The Philips 3T Intera MRI** from the institute for clinical radiology at the university hospital in Münster, which has been upgraded to a Achieva 3.0T with 'Quasar Dual'-Gradients, was used for data collection. The data collected from the MRI included both the magnitude and phase images. The scanner used the following setting:

- 3T field strength
- Sagittal imaging plane (of the liver)
- Pulse sequence: balanced Fast Field Echo (FFE)
- Acquisition trajectories: cartesian & radial
- Temporal resolution: 0.79s (cartesian) | 0.81s (radial)
- Echo time (TE): 2.63ms (cartesian) | 2.67ms (radial)
- Repetition time (TR): 5.27ms (cartesian) | 5.33ms (radial)
- Matrix size: 160x160
- Spatial resolution of: 1.875mm by 1.875mm with a slice thickness of 2mm

**Software** implementations of the synthetic MR image reconstruction algorithms were developed in Matlabs. PixelMed DicomeCleaner was used to anonymize the DICOM image files from the MR scanner. Software provided with the Optel Opbox was used for ultrasound data acquisition.

**The workstation specifications** are as followed: Samsung Ativ Book 8 laptop, Intel i7-3635QM processor, AMD Radeon HD8870M GPU, 10GB DDR3 RAM and 1TB Samsung 850 EVO SSD.

#### 4.2.5 Synchronisation of Surrogate Sensors

The synchronisation of the auxiliary sensors with the sampling of the MR image is an important component of this research to create a valid dataset. The US acquisition could not be triggered by the MRI, see section 5.1.3. Hence the synchronization accuracy is mostly dependant on the simultaneous pressing a button of the US and MRI. The respiratory bellow was synchronized by the instructor pressing hard on the bellow after the start signal was given.

#### 4.2.6 Participants & Available data

Table 2 shows the dataset which has been created with the breathing procedure. The data is stored per experiment but has also been segmented into per breathing activity files.

Each participant performed the breathing procedure twice in one session. The participants which performed the procedure in the MRI were first scanned with the pulse sequence using a cartesian trajectory. During the second breathing procedure they were scanned with a pulse sequence using a radial trajectory. In total five participants, three males and two females, performed the breathing procedure in the MRI.

**Table 2.** Participants and available data

| | | | | Available data | | |
|---|---|---|---|---|---|---|
| **ID** | **Age** | **Gender** | **BMI** | MRI | US | Respiratory Bellow |
| A | 33 | Male | 27.4 | Yes | Yes | No |
| B | 26 | Female | 20 | Yes | Yes | Yes |
| C | 26 | Male | 22.1 | Yes | Yes | Yes |
| D | 33 | Male | 24.4 | Yes | Yes | Yes |
| E | 25 | Female | 21.1 | Yes | Yes | Yes |
| F | 26 | Male | 26.9 | No | Yes | No |
| G | 26 | Male | 23.3 | No | Yes | No |
| H | 24 | Male | 21.7 | No | Yes | No |
| I | 27 | Male | 27.2 | No | Yes | No |
| J | 27 | Male | 19.7 | No | Yes | No |

### 4.3 Performance Metrics

Several performance metrics were used in order to measure the performance of the algorithms to generate synthetic MRI. This section lists these performance metrics that were used in this research.

Their usage is discussed in relation to other works on synthetic MRI formation and the end applications: target tracking and segmentation for automated robot (assisted) surgery.

### Normalized Mean Squared Error (NMSE)

Normalized Mean Squared Error (NMSE) is a pixel-wise comparison metric and can be used to measure the closeness of an estimate to a golden standard. NMSE is widely used, however it tends to favour smoothness over sharpness and therefore should not be used on its own [21]. Especially since target tracking and segmentation benefit from sharp details in the images. Lower NMSE values indicate better performance.

The reconstructed image $\hat{v}$ and reference image $v$ are used to calculate the NMSE score as shown in equation 3. The subtraction is performed entry-wise and the $\|\cdot\|_2^2$ is the squared Euclidean norm.

$$NMSE(\hat{v}, v) = \frac{\|\hat{v} - v\|_2^2}{\|v\|_2^2} \tag{3}$$

### Structural Similarity (SSIM)

Structural SIMilarity (SSIM) index is a block-level comparison metric where an area of pixels in two images is compared based on the local mean, standard deviation and cross-covariance of those pixels. In this research the Mean SSIM (M-SSIM) of all "blocks" was used. Target tracking and image segmentation benefit from this metric as this metric detects if areas in the image have the same structure. For example, in contrast to NMSE this metric will detect blurring [22]. A higher SSIM index indicates better performance. SSIM is computed by combining the luminance (l), contrast (c) and structural (s) terms.

$$SSIM(\hat{v}, v) = [l(\hat{v}, v)]^{\alpha} \cdot [c(\hat{v}, v)]^{\beta} \cdot [s(\hat{v}, v)]^{\gamma} \tag{4a}$$

*where*

$$l(x,y) = \frac{2\mu_x\mu_y + C_1}{\mu_x^2 + \mu_y^2 + C_1} \tag{4b}$$

$$c(x,y) = \frac{2\sigma_x\sigma_y + C_2}{\sigma_x^2 + \sigma_y^2 + C_2} \tag{4c}$$

$$s(x,y) = \frac{\sigma_{xy} + C_3}{\sigma_x\sigma_y + C_3} \tag{4d}$$

$\mu_x, \mu_y, \sigma_x, \sigma_y$ and $\sigma_{xy}$ are the local means, standard deviations and cross covariance of the input images. In this research an isotropic Gaussian with a standard deviation of 1.5 is used to weight the neighbourhood pixels around a pixel from which to calculate these local statistics. The constants $C_1, C_2$ and $C_3$ are used to prevent instability when the the local metrics approach zero. In this research they were calculated using the dynamic range $L$, being 1 for the gray-scale images with the range of 0 to 1, as follows: $C_1 = 0.01L$, $C_2 = 0.03L$ and $C_3 = C_2/2$.

### Perception-based Image Quality Evaluator (PIQE)

Perception-based Image Quality Evaluator (PIQE) is a no-reference image quality metric proposed in [23]. This algorithm determines the quality of an image based on the

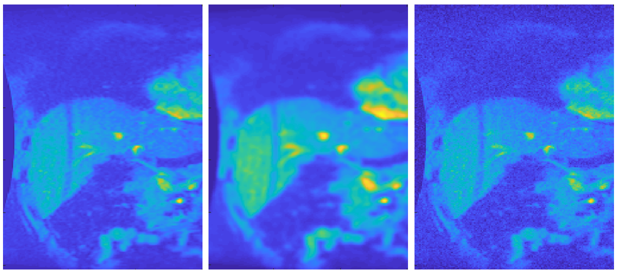

**(a)** Original **(b)** Blurred **(c)** Noised

**Figure 6.** Coronal liver-area MR image from the Preiswerk dataset [12] with different types of artifacts

human perception of distortions without prior knowledge of the images, hence no training dataset is required to train the algorithm. This enables evaluation of the image quality of synthetic MR images generated between samples. Other performance metrics cannot be used because these images do not have a ground-truth/reference image which is required for most metrics. Quality is estimated from block level metrics, but only for blocks that are found to be perceptually significant. A quality score (Qscore) is given to an image from 0 to 100 indicating good to bad quality respectively. Hence, lower Qscores are better. These scores correlate well to human subjective scores from several (non-MRI) image databases [23]. Table 3 shows the Qscore ranges and perceived quality.

**Table 3.** PIQE Qscore values and quality indication [24]

| Quality Scale | Qscore range |
|---|---|
| Excellent | [0, 20] |
| Good | [21, 35] |
| Fair | [36, 50] |
| Poor | [51, 80] |
| Bad | [81, 100] |

The metric has been used for MRI image quality evaluation [25] but was not tested on a dataset containing MR images with human subjective scores. It's also not made to detect MRI specific artifacts. 4 shows that the PIQE Qscores does indicate image quality lowering for blurred and noisy MR images as shown in Figure 6.

**Table 4.** PIQE Qscore average and standard deviation for sagittal liver-area MR images with added noise or blur from the open Preiswerk dataset [12]

| **Gaussian blur $\sigma$** | **0** | **0.5** | **1.0** | **1.5** |
|---|---|---|---|---|
| **Qscore $\mu$** | 24.7 | 30.9 | 65.5 | 86.7 |
| **Qscore $\sigma$** | 1.74 | 2.57 | 3.79 | 5.54 |
| | | | | |
| **Gaussian white noise $\sigma^2$** | **0** | **0.0005** | **0.0010** | **0.0015** |
| **Qscore $\mu$** | 24.7 | 38.6 | 52.2 | 58.1 |
| **Qscore $\sigma$** | 1.74 | 1.16 | 0.67 | 0.58 |

#### Smoothness - Spectral Arc Length (SAL)

The Spectral Arc Length (SAL) is a dimensionless measure for smoothness (of motion) first introduced by Balasubramanian *et al.* [26]. It measures smoothness by calculating the arc length of the Fourier magnitude spectrum of a speed profile. The speed profile contains the speed of an object over time. The metric operates on the following principal: more complex and less smooth motion will display a more complex magnitude spectrum with a longer arc length as seen in figure 7. The result is a negative number with numbers closer to zero indicating more smoothness. The SAL value for a motion with speed profile $v(t), t \in [0,T]$ and duration $T$ can be calculated as followed:

$$SAL \triangleq -\int_0^{\omega_c} \sqrt{\left(\frac{1}{\omega_c}\right)^2 + \left(\frac{d\hat{V}(\omega)}{d\omega}\right)^2}\, d\omega \tag{5a}$$

*where*

$$\hat{V}(\omega) \triangleq \frac{V(\omega)}{V(0)} \tag{5b}$$

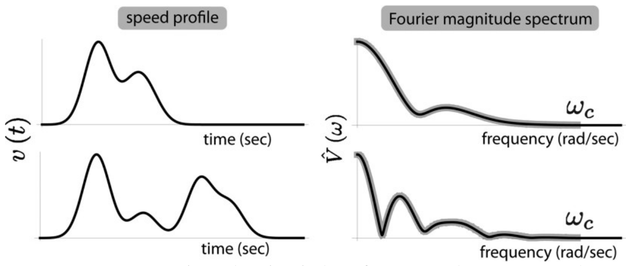


**Figure 7.** Operational principle of Spectral Arc Length (SAL). Left column: the speed profile of a more smooth (top) and less smooth (bottom) motion. Right column: the Fourier magnitude spectrum showing the spectral arc, the thick grey line, being shorter for the smoother (top) than the less smooth (bottom) motion. [26]

## 4.4 Pre- & Post-Processing

Several pre- and post-processing methods were applied to the MR images. This section describes the types which were applied.

### 4.4.1 DICOM Pre-Processing

The MR images are stored in the DICOM format which contains several parameters to pre-process the MR image. First the raw pixel values need to be rescaled according to the rescale slope and intercept parameters, see equation 6. After which the image is thresholded using the windows center (c) and window width (w) to convert it to display values, see equation 7. The display values minimum ($x_{min}$) and maximum ($x_{min}$) may be chosen arbitrarily.

$$x_{scaled} = (slope \cdot x_{raw}) + intercept \tag{6}$$

$$x_{display} = \begin{cases} x_{min} & \text{if } x_{scaled} <= c - 0.5 - \frac{(w-1)}{2} \\ x_{max} & \text{else if } x_{scaled} > c - 0.5 + \frac{(w-1)}{2} \\ x_{new} & \text{else} \end{cases} \tag{7a}$$

*where*

$$x_{new} = \left(\frac{x_{scaled} - (c-0.5)}{(w-1)} + 0.5\right) \cdot (x_{max} - x_{min}) + x_{min} \tag{7b}$$

### 4.4.2 Global Contrast Stretching (GCS)

Global Contrast Stretching (GCS) was used as a post-processing technique which improves the observed contrast. Gamma encoding is applied to an image (I) with $\gamma = 0.75$ in order to improve visual detail. Then, the image 0.2% saturation limits are computed and the image is saturated. Finally, the image is rescaled to the minimum (0.0) and maximum (1.0). This process can be seen in algorithm 1.

**Algorithm 1:** Global Contrast Stretching

**Data:** MR Image (I), saturation percentage (s), number of histogram bins (nBins)
**Result:** Global Contrast Stretched Image

```
/* Gamma encoding */
I = I.^0.75                               // element-wise square
I = rescale(I, [0,1])                     // rescale to gray-scale [0,1]
/* Find saturation limits */
hist = histogram(I, nBins)                // histogram
cdf = cumsum(hist)/sum(hist)              // cdf
limit_low = (find(cdf > s) - 1)/(nBins - 1)
limit_high = (find(cdf > 1 - s) - 1)/(nBins - 1)
/* saturate image */
I = saturate(I, [limit_low, limit_high])  // saturate & rescale
return I
```

### 4.4.3 De-hazing

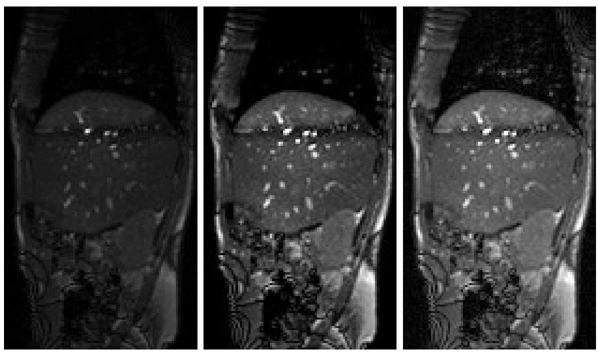

**(a)** Original **(b)** Pre-Processed **(c)** De-hazed

**Figure 8.** Coronal MR image of the liver

Without pre-processing the (magnitude) images appear to be dark and have low-dynamic range. Other research [27] found that de-hazing techniques can be applied to low-light/dark images to improve visibility and quality. De-hazing is normally used to improve images which are hazy due to fog or particles in the air. This research uses the dehazing technique as described in [28] which uses quad-tree decomposition to estimate the atmospheric light. Figure 8c shows this processing step applied on an MR image.

## 4.5 Enhancements

Next to pre- and post-processing other techniques were experimented with in order to improve synthetic MR image reconstruction performance. This section lists these proposed enhancements. The main issue with RIG and especially RKG is that the computation time for a synthetic MR image grows exponentially as more data is fed in.

### 4.5.1 Conjugate Symmetric K-space

This enhancement is only applicable to the RKG approach to synthetic MR image generation and attempts to exploit the conjugate symmetry of the k-space. Which would theoretically allow the whole k-space to be reconstructed by calculating the conjugate of half the k-space. Using half the k-space would allow a reduction in computation time or doubling the amount of samples per k-space line trajectory.

### 4.5.2 Locally-Sensitive Hashing (LSH)

Hashing is used to map data from an arbitrary size to a vector of fixed size which is usually much smaller. Locally-Sensitive Hashing (LSH) hashes similar data vectors to similar signature vectors. A similarity function can be used in order to calculate the similarity between two signatures. In this research random projection LSH was implemented as seen in algorithm 2.

LSH can be used as an enhancement for RIG and RKG in order to reduce computation time by reducing the number of similarity weights that need to be calculated. This is done by calculating signatures for all historical datapoints. Then, LSH is used to obtain the $K_{lsh}$ most similar datapoints, which are calculated relatively fast, when a synthetic image needs to be generated. After which the normal similarity weights for RIG and RKG are calculated, which is relatively slow, to generate the synthetic image.

**Algorithm 2:** Random Projection Locally-Sensitive Hashing

**Data:** UltrasoundWindow1, UltrasoundWindow2, hashSize=24, dataSize=10000
**Result:** SimHash

$randProj = getRandomProjection(hashSize, dataSize)$
$sig1 = getSignature(randProj, UltrasoundWindow1)$
$sig2 = getSignature(randProj, UltrasoundWindow2)$
$simhash = getSimHash(sig1, sig2)$
**return** $simHash$

**Function** *getRandProjection(sizeOut, sizeIn)*:
  `/* Generate matrix of uniform random numbers ranging from [-1,1] of size [sizeOut, sizeIn] */`
  **return** $-1 + 2 \cdot uniformRandom(sizeOut, sizeIn)$
**end**

**Function** *getSignature(randProj, inputVector)*:
  `/* Generate signature of size [sizeOut] bits from input vector of size [sizeIn] */`
  **return** $(randProj \cdot inputVector) >= 0$
**end**

**Function** *getSimHash(N, signature1, signature2)*:
  $xorVector = xor(signature1, signature2)$
  $nnzValue = numberOfNonZerosValues(xorVector)$
  **return** $(N - nnzValue)/N$
**end**

## 4.6 Experiments

Several performance metrics were used in order to measure the performance of the algorithms to generate synthetic MRI. This section will discuss how these performance metrics were interpreted. The terms RM, breathing and activity are used interchangeably.

### 4.6.1 Performance Per Activity

The performance per activity is evaluated for both the retrospective image and k-space gating approaches.This analysis uses the cartesian MR images and US data of one breathing-type and feeds them to the algorithms generating synthetic MRI. The algorithms learns from this data and generate a synthetic output image. The algorithms are implemented online and hence have no prior knowledge of the image they are trying to approximate. The performance metrics, except smoothness, are calculated when a reference MR image is available. This is repeated for every breathing-type. Breathing-type is occasionally referred to as activity in the statistical analysis.

An repeated measures ANalysis Of VAriance (ANOVA) using a General Linear Model (GLM) was performed in order to conclude there is a statistically significant difference in performance between different activities. The GLM contained the following terms: breathing-type, participant identity (id) and the interaction of these terms (breathing-type*id). Then Tukey's method is used to generate confidence intervals for the differences in mean performance per breathing-type. With this information it can be concluded if the performance between two activities is significantly different.

The first 15 seconds of the output is not considered in the statistical analysis. This is done to allow the algorithm to initialize and start learning. The last 15 seconds are not considered, except for the coughing breathing-type, to insure that there is no contamination from another activity in the data.

### 4.6.2 Image Versus K-space Gating

Retrospective Image Gating (RIG) is compared to Retrospective K-space Gating (RKG). This comparison also looks at the difference in performance per activity. The cartesian

MRI subset is used as input for the algorithms.

Interval plots with a confidence interval of 95% of the performance metrics are created to show the difference in performance per algorithm and per activity. Smoothness is evaluated separately from the other metrics in order to visualize and observe temporal changes better. The SAL metric is calculated with a sliding window of 10 seconds wide in order to generate a speed profile that changes over time. The first window is from 5 to 15 seconds after the start of the MRI sequence. Optical flow vectors are calculated by applying Lukas-Kanade optical flow tracking to the area of liver motion in order to calculate the speed profile [29]. The motion in the Z direction (Head-to-Toe) of the liver images is used for the speed profile. Smooth liver motion is expected for the regular breathing type due to the calm nature of this breathing type.

## 5. Results & Discussion

### 5.1 Data Acquisition

Table 2 shows the dataset which has been created with the breathing procedure. The respiratory bellow data was not available for participant A and all the participants who did not perform the experiment in the MRI. Participant E misses the last 6.5 second of coughing in the US data. Participant C was breath-holding at the end-of-inhalation instead of at the end-of-exhalation during the acquisition of the cartesian MR images.

Several experiments which were conducted in order to try and find appropriate methods and materials failed to live up to expectations or requirements. These failures in some cases delayed the research. This section will discuss the gained experience as well as the cause and solution to failures.

#### 5.1.1 Using a digital oscilloscope as a digitizer

Initially two attempts were made to use an oscilloscope as a digitizer for the ultrasound signal in the setup as shown in Figure 9 with an Olympus 5077PR for the pulser/receiver. The first attempt used the Link Instruments DSO-8500 connected to a PC as digitizer. This setup failed due to oscilloscope dead time: "The time between each repetitive acquisition of the scope when it is processing the previously acquired waveform" [30]. Dead time caused the oscilloscope to miss triggers when the pulse repetition frequency (PRF) of the ultrasound transducer was set any higher than 1 Hz due to the time that was required to show and store the ultrasound waveform; this frequency is well below the required PRF. This problem was initially solved by using the Rohde & Schwarz RTB2000 oscilloscope. This oscilloscope allowed the collection of two minutes of ultrasound data at 100Hz or 20 minutes at 10Hz by using the segmented memory function to increase the amount of samples that can be buffered and the fast segmentation function to reduce dead time. However, permanently storing the data to USB takes 5 to 6 hours if the full history buffer is filled and no other outputs were available with the segmented memory function. This reduced the practical usage of this setup when using an MRI; which is considered a limited resource. This initiated the decision to look for another solution which resulted in the purchase of the Optel Opbox and transducers used in this research.

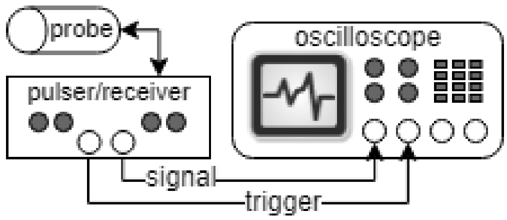


**Figure 9.** Oscilloscope setup

#### 5.1.2 Ultrasound transducer

Initially, work was to be done with an MR-SAFE Imasonic cdc12239-5 7.5MHz ultrasound transducer. However, this transducer did not arrive and instead transducer with metal encasing arrived which is unsuitable as an surrogate during MRI acquisition. This issue also initiated the decision to look for another solution which resulted in the purchase of the Optel Opbox and transducers used in this research.

#### 5.1.3 MRI

It was intended to trigger the US pulser/receiver by a trigger pulse from the MRI. This trigger pulse was present, however only once per image instead of once per k-space line or other higher frequency process. This forced us to set a constant PRF on the Optel Opbox.

The first day of experiments would require setting up the MRI, this included finding the right parameters and pulse sequence which would meet the requirements. This required a large portion of the day, more time than expected, and resulted in a second day of experiments with the MRI.

#### 5.1.4 Breathing procedure

Time restraints with the use of the MRI forced the initial breathing procedure to be shortened. This resulted in shorter segments for each breathing type and the removal of the recovery segment between regular breathing and breath holding. The latter is not an issue since during try-outs it was found that people did not require rest after regular breathing and the fact that some regular breathing was already going to be present in the breath-hold segment. However, this did make several ultrasound-only experiments unpractical to use and hence were discarded after which new ones were made. Another time constraint was found with the coughing breathing type; participants were regularly not able to comfortably induce coughing for more than 30 seconds and hence this section was also shortened.

Breathing instructions needed to be given clearly and repetitively, complex instructions were found to result in unreliable execution. A surprising observation was made regarding the instruction to start the recovery segment. In try-out

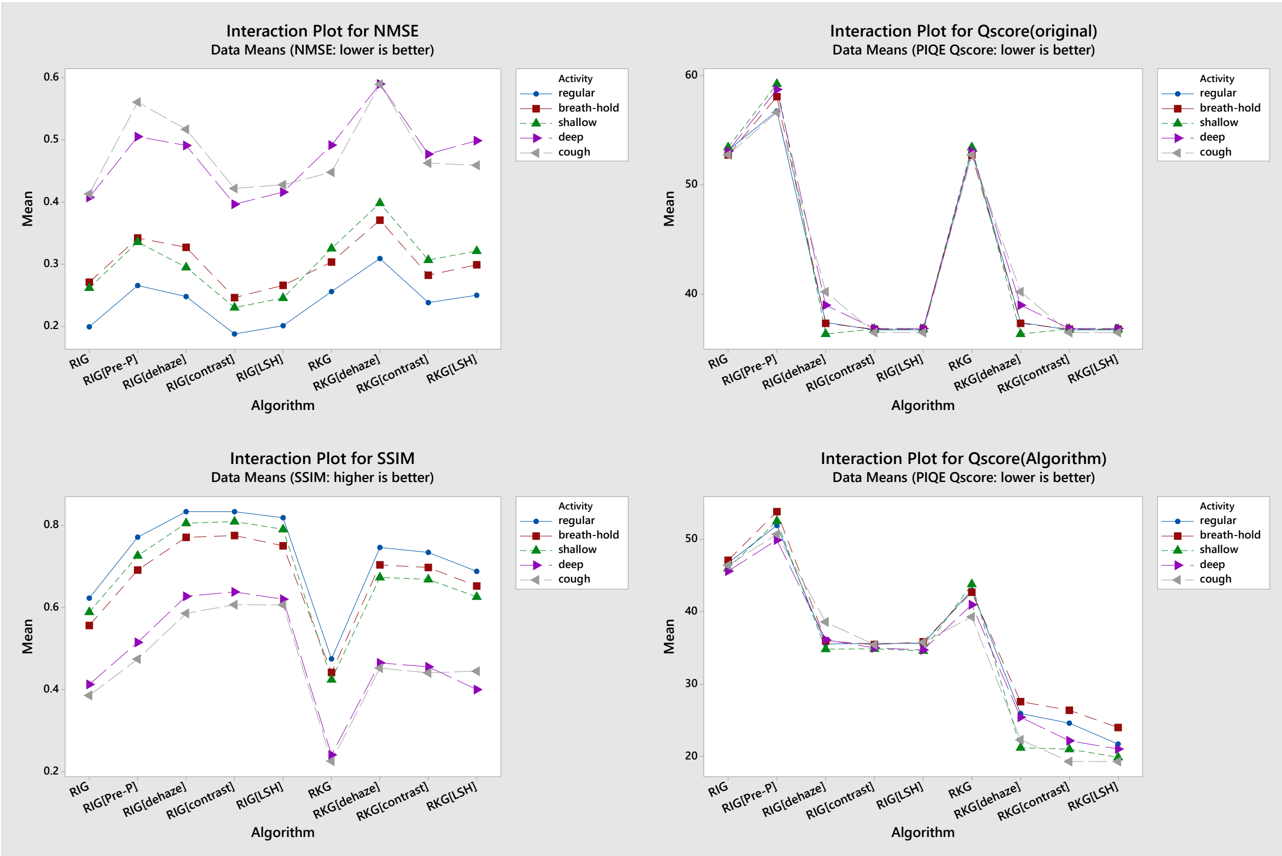


**Figure 10.** Interaction plots of performance metrics generated by the RIG and RKG algorithms

experiment the participants reacted more instinctively when instructed to "relax" than when the instruction "recover", "normal breathing" or "regular breathing" was given and hence it is advisory to use this form.

Another complication arose when it was found that it would not be possible to give instructions to someone during the experiment due to the loudness of the MRI. Hence the instructions were printed on paper and

Originally it was intended to give the breathing instructions over a headphone to the participant during the experiment. However, no such headphone was available and the loudness of the MRI would also make it hard for the participant to understand speech. Hence instructions were printed on paper and shown to the participant during the experiment. The instructor would squeeze the participants leg at the start of a breathing segment in order to notify the participant.

### 5.2 Pre- & Post-Processing

This section will compare the RIG and RKG algorithms with and without DICOM pre-processing (Pre-P) using the window width and center parameters in the DICOM file, examples are shown in figure 8a and 8b. Figure 10 shows an interaction plot between algorithms, breathing type (activity) and pre/post-processing.

The RIG algorithm performs worse on the NMSE and PIQE metrics when pre-processing is enabled. However, the SSIM metric improves. A side effect of disabling the pre-processing step is that the generated video has a varying overall brightness making the video seem to flicker. Human perception of the generated synthetic MRI video is better with the pre-processing enabled. Supposedly, the original algorithm was also developed with DICOM pre-processing. The effect is caused by the fact that the input images have different brightnesses and contrasts without pre-processing, since the algorithm learns from these images it also generates images with varying brightness. An issue with the DICOM pre-processing is that this step can only be applied to the input MR images and cannot be applied to the generated synthetic images.

Figure 10 also shows the performance metrics for the GCS (contrast) and de-hazing [27] post-processing techniques. Only GCS improves the NMSE score for most breathing types compared to standard RIG and RKG. The SSIM score is improved by all pre- or post-processing. The objective image quality measured by PIQE of the original MR images is improved by all post-processing techniques. Pre-processing reduces PIQE(algorithm output) performance. The same results are observed for the PIQE score of the synthetic images (PIQE algorithm).

## 5.3 Enhancements

### 5.3.1 Conjugate Symmetric K-space

The enhancement exploiting the conjugate symmetric property of the k-space failed to produce any sensible images due to the following issues. The k-space center was shifted in most of the MR images, likely due to inhomogeneity in the magnetic field of the MR scanner. An attempt was made to fix this issue by cropping the k-space and shifting it back to the center, resulting in reduced spatial resolution as some higher frequencies got thrown away. However, this still did not allow the exploitation of the conjugate symmetric property as the k-space was still not conjugate symmetric possibly due to the center frequency lying between pixels in the k-space.

### 5.3.2 Locally-Sensitive Hashing

The performance compared to the other implementations of the RIG and RKG algorithms can be seen in figure 10. No large differences in performance between LSH enhanced implementations and the other post-processed implementations are observed. Table 5 shows the computation times for the RIG and RKG algorithms with or without the LSH enhancement on 2 minutes of MR images and ultrasound data. The signature size was empirically set to 24 bits and $K_{lsh}$ was set to 40.

**Table 5.** Average total execution time (s) of RIG and RKG with and without LSH on 120 seconds of data

| | Standard | with LSH | Improvement |
|---|---|---|---|
| RIG | 111 | 89 | 20% |
| RKG | 9562 | 4740 | 50% |

The RIG and RKG implementation both generated synthetic MR images at 50Hz for 120 seconds of data. The RIG implementation is able to generate these images in less than 120 seconds with and without LSH, however the RKG algorithms requires much more processing time. The LSH enhancement reduces the computation time by 50% for RKG however this is still above the 120 seconds of time it took for the original data to be recorded.

Table 5 shows the total execution time for both algorithms, however it does not measure the delay between the time a datapoint, MR image and US, is coming in and the time a synthetic image is generated. This delay is also growing as more data is fed into the algorithms. It was observed that the LSH enhancement pre-selecting $K_{lsh}$ similar historical datapoints caps the growth in the execution time per synthetic image depending on the chosen $K_{lsh}$ value.

## 5.4 Performance Per Activity

### 5.4.1 Retrospective Image Gating

Appendix B shows several plots and statistical analyzes on the performance metrics per activity which are discussed below. The output of the algorithm is post-processed with the de-hazing algorithm. Table 6 shows the averages of the performance metrics per breathing type.

**Table 6.** Average RIG[dehaze] performance

| | NMSE | SSIM | PIQE(O) | PIQE(RIG) | PIQE(RIG-O) |
|---|---|---|---|---|---|
| **regular** | 0.25 | 0.83 | 37.39 | 35.54 | -1.85 |
| **breath hold** | 0.33 | 0.77 | 37.31 | 35.97 | -1.35 |
| **shallow** | 0.30 | 0.81 | 36.33 | 34.81 | -1.53 |
| **deep** | 0.49 | 0.63 | 38.98 | 36.12 | -2.86 |
| **cough** | 0.53 | 0.58 | 40.40 | 38.64 | -1.76 |
| **Average** | 0.38 | 0.72 | 38.08 | 36.21 | -1.87 |

Appendix B.1 shows the histograms of the calculated performance metrics per activity for the RIG algorithm. The histograms include a normal distribution fitted to the data for which the parameters are displayed. Appendix B.2 shows the results from the repeated measures ANOVA. The residuals for SSIM are normally distributed, but the NMSE and PIQE residuals are skewed. However, ANOVA still works well if the residuals are not highly skewed [31]. Appendix B.3 shows if the averages of a performance metric for two breathing types is statistically different with a 95% confidence interval.

The NMSE histogram indicates that regular breathing shows the best performance followed by shallow breathing and breath-holding. Deep breathing and coughing perform significantly worse. Appendix B.3 shows that we cannot proof that breath-holding and shallow breathing have significantly different means. All other combinations of breathing have significantly different performance.

SSIM indicates that regular breathing again shows the best performance. Followed by shallow and breath-holding. Again, deep breathing and coughing perform significantly worse. Appendix B.3 shows that all combinations of breathing type have significantly different performance.

Using appendix B.1 we can compare the difference between the PIQE Qscores of the original reference image to those generated by RIG. The images generated by RIG have better Qscores for all activities than the original images. Appendix B.4 confirms that the mean Qscores are different with a 95% confidence interval.

### 5.4.2 Retrospective K-Space Gating

Appendix C shows several plots and statistical analyzes on the performance metrics per activity which are discussed below. The output of the algorithm is post-processed with the de-hazing algorithm. Table 7 shows the averages of the performance metrics per breathing type.

**Table 7.** Average RKG[dehaze] performance

| | NMSE | SSIM | PIQE(O) | PIQE(RKG) | PIQE(RKG-O) |
|---|---|---|---|---|---|
| **regular** | 0.31 | 0.75 | 37.39 | 25.92 | -11.46 |
| **breath hold** | 0.37 | 0.70 | 37.31 | 27.56 | -9.75 |
| **shallow** | 0.40 | 0.67 | 36.33 | 21.21 | -15.13 |
| **deep** | 0.59 | 0.46 | 38.98 | 25.43 | -13.55 |
| **cough** | 0.60 | 0.45 | 40.40 | 22.39 | -18.01 |
| **Average** | 0.45 | 0.61 | 38.08 | 24.50 | -13.58 |

Appendix C.1 shows the histograms of the calculates performance metrics per activity for the RKG algorithm. The histograms include a normal distribution fitted to the data for which the parameters are displayed. Appendix C.2 shows the results from the repeated measures ANOVA. All residuals are seem normally distributed. Appendix C.3 shows if the averages of a performance metric for a combination of two breathing types is statistically different with a 95% confidence interval.

The NMSE histogram indicates that regular breathing shows the best performance followed by breath-holding and shallow breathing. Coughing and deep breathing seem to perform significantly worse. Appendix C.3 shows that there is statistical evidence to state that all NMSE performances are significantly different except the difference in means of coughing and deep breathing.

The SSIM histogram indicates that regular breathing shows the best performance followed by breath-holding and shallow respectively. Deep breathing and coughing follow, seemingly significantly worse. Appendix C.3 supports these statements, however a significant difference in performance between deep breathing and coughing is not observed.

While looking at the PIQE Qscores in appendix C.4 it can be concluded that the RKG algorithm performs significantly better than the original MR images.

### 5.5 RIG Versus RKG

Figure 11 shows the output of the RIG and RKG algorithms after training on two minutes of regular breathing. Visually it is difficult to see differences between the RIG and RKG output, but both of them smooth out the noise in the darker areas when compared to the original MR image.

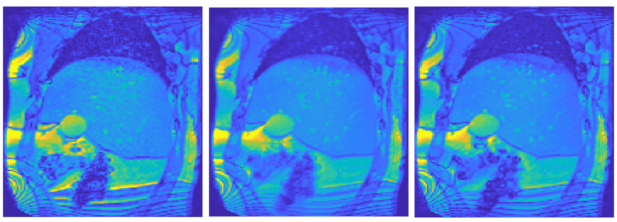

**(a)** Original **(b)** RIG **(c)** RKG

**Figure 11.** Original and synthetic MR images after two minutes of training on regular breathing of participant D

Figure 10 shows that RIG performs significantly better, with a 95% confidence interval, on the NMSE and SSIM metrics for all activities. The RKG algorithm performs better on the PIQE metric. Appendix D.1 interval plots confirm these observations. Table 8 also shows the differences in average performances per metric between RIG and RKG.

**Table 8.** Difference in performance metrics (RKG - RIG). Red indicates better performance for RIG and green indicates better performance of RKG.

| | NMSE | SSIM | PIQE(algorithm) |
|---|---|---|---|
| **regular** | 0.06 | -0.09 | -9.61 |
| **breath hold** | 0.04 | -0.07 | -8.40 |
| **shallow** | 0.10 | -0.13 | -13.60 |
| **deep** | 0.10 | -0.16 | -10.69 |
| **cough** | 0.08 | -0.13 | -16.25 |
| **average** | 0.08 | -0.12 | -11.71 |

Figure 12 shows the smoothness metric SAL over time. The RKG algorithm is overall showing smoother liver motion than RIG and is getting better smoothness scores faster. The RIG algorithm could be converging towards a similar value. Execution time is significantly higher for RKG than for RIG as shown in table 5.

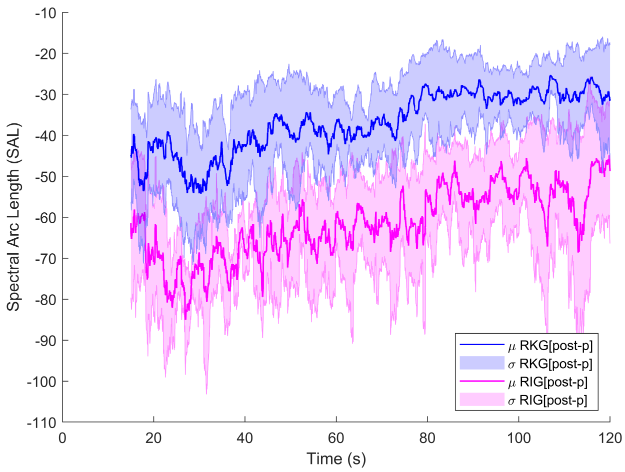


**Figure 12.** Spectral Arc Length (SAL) over time for regular breathing. The mean $\mu$ and standard deviation $\sigma$ are calculated for participants A to E. A higher SAL value indicates smoother motion.

## 6. Limitations

### MRI as Gold Standard

The original MR images are used as a gold standard in this research. However, MR images are subject to several types of artifacts and therefore is not a perfect reference. In this research the MR imaging was performed with participants who were free-breathing, hence causing RM. The pulse sequence which was used, balanced SSFP, is especially susceptible to SSFP banding which are also known as "B0 Banding Artifacts". These are observed in the dataset as bands, mostly emanating from the outside corners of the image.

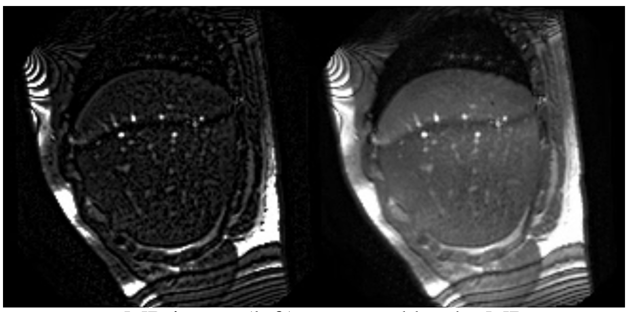

**Figure 13.** MR image (left) generated by the MR scanner and its counterpart synthetic image generated with the RIG algorithm (right). The liver in the left image appears much darker than it should be when compared to other images in the sequence.

Figure 13 shows a situations were the original MR image does not seem to be a good reference. The reference MR image is too dark when compared to the rest of the of the MR images in the sequence. Hence, in this case the synthetic image is possibly of better quality then the original reference. This is also an argument for using the non-reference error metric PIQE.

### PIQE Metric for MRI

The PIQE metric tries to quantify the perceived quality by a person looking at an image. However, this metric does not take into account the same considerations that medical personal have when evaluating an MR image. Also, MRI artifacts are not considered by this metric.

### Breathing Procedure - Coughing

Less data for the coughing breathing type is available than for the other breathing types as participants were regularly not able to comfortably induce coughing for more than 30 seconds. As the synthetic MR image reconstruction algorithms have less data to learn from performance is inherently reduced.

### MRI & Ultrasound Synchronization

It was not possible to trigger US acquisition with the trigger from the MR scanner due to the limitations of the scanner. The scanner was only capable of sending a trigger pulse once per image instead of once per k-space line, however this would have resulted in a low acquisition rate for the US. Hence, a constant PRF of 50 Hz was set, however therefore the initial start trigger for both the US and MRI was performed with the push of two buttons by a person. It was assumed that the difference between the start time of MRI and US was within a second, however the only way to check this assumption was by human observation of the data afterwards. This inaccuracy was reduced by performing all breathing types in one procedure instead of one by one, hence requiring only one start trigger for all breathing types procedure.

## 7. Conclusions

This research focused on evaluating online synthetic MR image reconstruction techniques for different types of breathing. A data acquisition procedure was developed and executed in order to asses MRI and US sensor fusion with the possibility of evaluating future work focused on respiratory motion classification and prediction by the labelling of the data. Five participants performed the procedure inside the MRI and another five performed the procedure without the MRI. Performance metrics were chosen based on literature and practical observation of the issues displayed in the generated synthetic MR images. The metrics NMSE, SSIM and PIQE were chosen to represent pixel-wise similarity, block-level similarity and objective image quality respectively. SAL was added in order to visualize how the online RIG and RKG algorithms produced smoother motion of the liver over time as they learned from incoming data.

Both algorithms, RIG and RKG, perform best with regular breathing followed by breath-holding and shallow. Deep breathing and coughing perform significantly worse, which is likely due to the fact that they contain more states of motion requiring more training data. However, there is also significantly less coughing data available for the algorithm to train on. Another factor is that the speed of motion for deep breathing and coughing is higher and therefore also generates more artifacts in the input MR images.

Pre- and post-processing increased the performance on the SSIM and PIQE metrics while reducing it for the NMSE metric. This indicates that observed quality and block-level similarity is better however the pixel by pixel differences between the original MR image and the synthetic one are larger. A major side effect from the pre- and post-processing is that the overall brightness in the generated synthetic video became more stable, where without pre- or post-processing the overall brightness would seem to flicker.

The LSH enhancement improved computation time by 20% for RIG and 50% for RKG and hence presents a significant improvement to especially the RKG algorithm regarding real-time operation. An important contribution of the LSH enhancement is that it caps the growth in execution time per synthetic image as more data is being fed in.

The proposed RIG approach performed better compared to the RKG approach according to the NMSE and SSIM metrics. However, the RKG approach performed better on the PIQE metric indicating that perceived image quality is higher. This approach also generated a smoother synthetic video according to the SAL metric. This indicates that the algorithm learns faster and displays a more accurate representation of the real motion which is important for target tracking.

### Future work

Future work will need to focus on applying the currently presented techniques for synthetic MR image creation with surgical equipment, target segmentation and tracking. A b-mode ultrasound sensor could be used to scan the area where a surgical needle or probe is inserted. Then the needle could be shown at its current location on the generated synthetic image by using a feature detection algorithm like SIFT to match the generated MR and ultrasound image.

Computation time has been a significant issue during this research, with the computation time becoming longer per synthetic image as the history databases grows. Generating synthetic images for the whole breathing procedure with the original RKG implementation has an unknown computation time as computation was not halfway completed after 12 hours, with computation time per synthetic image still increasing. Another issue with the RIG and RKG approaches is that they do not reject MR images which contain artifacts or are otherwise of poor quality. These images contaminate the history database presumably resulting in lower performance.

Different MRI scanning trajectories could be evaluated with the RKG approach. MR images measured with a radial scanning trajectory were acquired in this research, but were not evaluated. An improved performance expected as radial scanning measures the k-space center frequencies, which contain the most information, with every measurement which could be used to compensate for respiratory motion. However, without any processing this trajectory suffers from more respiratory motion artifacts as the center of k-space is sampled over multiple parts of the respiratory cycle.

## Acknowledgments

I would like to thank my supervisors Ferdi van der Heijden, Momen Abayazid, Hamid Naghibi Beidokhti and Beril Sirmaçek for their guidance and advice during this research, as well as Frank Simonis for sharing his knowledge on MRI. Next, I want to thank Cornelius Faber, Nina Nagelmann and Harald Kugel from the university hospital of Münster for their cooperation and allowing us to use their facilities. I also want to show my appreciation to all the participants of the experiments for their time and willingness to help. Lastly, I want to express my immense gratitude to my family, friends and especially girlfriend, Saskia Hildebrandt, who have always supported and motivated me.

## References

[1] D. Li, J. Kang, B. J Golas, V. W Yeung, and D. Madoff, "Minimally invasive local therapies for liver cancer", *Cancer biology & medicine*, vol. 11, pp. 217–36, Dec. 2014. DOI: 10.7497/j.issn.2095-3941.2014.04.001.

[2] F. Bray, J. Ferlay, I. Soerjomataram, R. L. Siegel, L. A. Torre, and A. Jemal, "Global cancer statistics 2018: Globocan estimates of incidence and mortality worldwide for 36 cancers in 185 countries", *CA: A Cancer Journal for Clinicians*, vol. 68, no. 6, pp. 394–424, Dec. 2018. DOI: 10.3322/caac.21492.

[3] M. A. Clifford, F. Banovac, E. Levy, and K. Cleary, "Assessment of hepatic motion secondary to respiration for computer assisted interventions", *Computer Aided Surgery*, vol. 7, no. 5, pp. 291–299, Jan. 2002. DOI: 10.3109/10929080209146038. [Online]. Available: https://doi.org/10.3109/10929080209146038.

[4] A. D. Elster. (2018). Mri questions & answers; mr imaging physics & technology, [Online]. Available: https://mriquestions.com/index.html (visited on 02/04/2019).

[5] A. P. Matos, "Focal liver lesions: Practical magnetic resonance imaging approach", *World Journal of Hepatology*, vol. 7, no. 16, p. 1987, 2015. DOI: 10.4254/wjh.v7.i16.1987. [Online]. Available: https://doi.org/10.4254/wjh.v7.i16.1987.

[6] E. K. Brodsky, E. M. Bultman, K. M. Johnson, D. E. Horng, W. R. Schelman, W. F. Block, and S. B. Reeder, "High-spatial and high-temporal resolution dynamic contrast-enhanced perfusion imaging of the liver with time-resolved three-dimensional radial MRI", *Magnetic Resonance in Medicine*, vol. 71, no. 3, pp. 934–941, Mar. 2013. DOI: 10.1002/mrm.24727. [Online]. Available: https://doi.org/10.1002/mrm.24727.

[7] L. Vu, J. Morelli, and J. Szklaruk, "Basic mri for the liver oncologists and surgeons", *Journal of Hepatocellular Carcinoma*, vol. Volume 5, pp. 37–50, Apr. 2018. DOI: 10.2147/jhc.s154321.

[8] A. Giger, M. Stadelmann, F. Preiswerk, C. Jud, V. D. Luca, Z. Celicanin, O. Bieri, R. Salomir, and P. C. Cattin, "Ultrasound-driven 4d MRI", *Physics in Medicine & Biology*, vol. 63, no. 14, p. 145 015, Jul. 2018. DOI: 10.1088/1361-6560/aaca1d. [Online]. Available: https://doi.org/10.1088/1361-6560/aaca1d.

[9] M. Berijanian, *Estimation of hepatic tumors respiratory motion using learning algorithms and surrogates*, Oct. 2018.

[10] S. Fahmi, F. F. Simonis, and M. Abayazid, "Respiratory motion estimation of the liver with abdominal motion as a surrogate", *The International Journal of Medical Robotics and Computer Assisted Surgery*, vol. 14, no. 6, L. Clive, Ed., e1940, Aug. 2018. DOI: 10.1002/rcs.1940. [Online]. Available: https://doi.org/10.1002/rcs.1940.

[11] M. Abayazid, T. Kato, S. G. Silverman, and N. Hata, "Using needle orientation sensing as surrogate signal for respiratory motion estimation in percutaneous interventions", *International Journal of Computer Assisted Radiology and Surgery*, vol. 13, no. 1, pp. 125–133, Jan. 2018, ISSN: 1861-6429. DOI: 10.1007/s11548-017-1644-z. [Online]. Available: https://doi.org/10.1007/s11548-017-1644-z.

[12] F. Preiswerk, M. Toews, C.-c. Cheng, J.-y. G. Chiou, C.-S. Mei, L. F. Schaefer, W. S. Hoge, B. M. Schwartz, L. P. Panych, and B. Madore, "Hybrid mri-ultrasound acquisitions, and scannerless real-time imaging", *Magnetic resonance in medicine*, vol. 78, no. 3, pp. 897–908, 2017.

[13] K. Shokry, *Generating high frame rate mri images using a surrogate signal: Supervised learning approach*, Sep. 2018. [Online]. Available: http://essay.utwente.nl/76692/.

[14] J. M. Mislow, A. J. Golby, and P. M. Black, "Origins of intraoperative mri", *Neurosurgery Clinics of North America*, vol. 20, no. 2, pp. 137–146, 2009, Intraoperative MRI in Functional Neurosurgery, ISSN: 1042-3680. DOI: https://doi.org/10.1016/j.nec.2009.04.002. [Online]. Available: http://www.sciencedirect.com/science/article/pii/S1042368009000102.

[15] *Mri and ultrasound robotic assisted biopsy*. [Online]. Available: https://www.murabproject.eu/ (visited on 01/22/2019).

[16] V. Groenhuis, F. Siepel, J. Veltman, and S. Stramigioli, "Design and characterization of stormram 4: An mri-compatible robotic system for breast biopsy", English, in *2017 IEEE/RSJ International Conference on Intelligent Robots and Systems (IROS)*, United States: IEEE, Sep. 2017, pp. 928–933, ISBN: 978-1-5386-2683-2. DOI: 10.1109/IROS.2017.8202256.

[17] H. Lal, Z. Neyaz, A. Nath, and S. Borah, "CT-guided percutaneous biopsy of intrathoracic lesions", *Korean Journal of Radiology*, vol. 13, no. 2, p. 210, 2012. DOI: 10.3348/kjr.2012.13.2.210. [Online]. Available: https://doi.org/10.3348/kjr.2012.13.2.210.

[18] B. Chen, N. Weber, F. Odille, C. Large-Dessale, A. Delmas, L. Bonnemains, and J. Felblinger, "Design and validation of a novel MR-compatible sensor for respiratory motion modeling and correction", *IEEE Transactions on Biomedical Engineering*, vol. 64, no. 1, pp. 123–133, Jan. 2017. DOI: 10.1109/tbme.2016.2549272. [Online]. Available: https://doi.org/10.1109/tbme.2016.2549272.

[19] A. Giger, M. Stadelmann, F. Preiswerk, C. Jud, V. De Luca, Z. Celicanin, O. Bieri, R. Salomir, and P. C. Cattin, "Ultrasound-driven 4d mri", *Physics in Medicine & Biology*, vol. 63, no. 14, p. 145 015, 2018.

[20] K.-N. Vu, A. G. Haldipur, A. T.-H. Roh, P. Lindholm, and A. M. Loening, "Comparison of end-expiration versus end-inspiration breath-holds with respect to respiratory motion artifacts on t1-weighted abdominal mri", *American Journal of Roentgenology*, vol. 212, no. 5, pp. 1024–1029, 2019. DOI: 10.2214/ajr.18.20239.

[21] J. Zbontar, F. Knoll, A. Sriram, M. J. Muckley, M. Bruno, A. Defazio, M. Parente, K. J. Geras, J. Katsnelson, H. Chandarana, Z. Zhang, M. Drozdzal, A. Romero, M. Rabbat, P. Vincent, J. Pinkerton, D. Wang, N. Yakubova, E. Owens, C. L. Zitnick, M. P. Recht, D. K. Sodickson, and Y. W. Lui, "Fastmri: An open dataset and benchmarks for accelerated MRI", *CoRR*, vol. abs/1811.08839, 2018. arXiv: 1811.08839. [Online]. Available: http://arxiv.org/abs/1811.08839.

[22] Z. Wang, A. Bovik, H. Sheikh, and E. Simoncelli, "Image quality assessment: From error visibility to structural similarity", *IEEE Transactions on Image Processing*, vol. 13, no. 4, pp. 600–612, Apr. 2004. DOI: 10.1109/tip.2003.819861.

[23] Venkatanath N, Praneeth D, Maruthi Chandrasekhar Bh, S. S. Channappayya, and S. S. Medasani, "Blind image quality evaluation using perception based features", in *2015 Twenty First National Conference on Communications (NCC)*, Feb. 2015, pp. 1–6. DOI: 10.1109/NCC.2015.7084843.

[24] Mathworks. (). Perception based image quality evaluator (piqe) no-reference image quality score - matlab piqe, [Online]. Available: https://nl.mathworks.com/help/images/ref/piqe.html (visited on 02/04/2019).

[25] A. Cristobal-Huerta, D. Poot, M. Vogel, G. Krestin, and J. Hernandez-Tamames, "Compressed sensing 3d-grase for faster high-resolution mri", *Magnetic Resonance in Medicine*, vol. 0, no. 0, DOI: 10.1002/mrm.27789. eprint: https://onlinelibrary.wiley.com/doi/pdf/10.1002/mrm.27789. [Online]. Available: https://onlinelibrary.wiley.com/doi/abs/10.1002/mrm.27789.

[26] S. Balasubramanian, A. Melendez-Calderon, and E. Burdet, "A robust and sensitive metric for quantifying movement smoothness", *IEEE Transactions on Biomedical Engineering*, vol. 59, no. 8, pp. 2126–2136, 2012. DOI: 10.1109/tbme.2011.2179545.

[27] X. Dong, G. Wang, Y. Pang, W. Li, J. Wen, W. Meng, and Y. Lu, "Fast efficient algorithm for enhancement of low lighting video", *2011 IEEE International Conference on Multimedia and Expo*, 2011. DOI: 10.1109/icme.2011.6012107.

[28] D. Park, H. Park, D. K. Han, and H. Ko, "Single image dehazing with image entropy and information fidelity", *2014 IEEE International Conference on Image Processing (ICIP)*, 2014. DOI: 10.1109/icip.2014.7025820.

[29] B. D. Lucas and T. Kanade, "An iterative image registration technique with an application to stereo vision (ijcai)", vol. 81, Apr. 1981.

[30] *What is waveform update rate and why does it matter?* [Online]. Available: https://www.keysight.com/main/editorial.jspx?ckey=2342706&id=2342706&nid=-11143.0.00&lc=dut&cc=NL.

[31] *Does the response need to follow a normal distribution?* [Online]. Available: https://support.minitab.com/en-us/minitab/18/help-and-how-to/modeling-statistics/anova/supporting-topics/anova-models/does-the-response-need-to-be-normal/ (visited on 08/15/2019).

# Appendices

## A Pulser/Receiver House Of Quality

QFD: House of Quality
Project: Pulser Receiver Manufacturer with digitizer Comparison
Revision: 1
Date: 29/04/19

| Correlations | |
|---|---|
| Positive | + |
| Negative | − |
| No Correlation | |

| Relationships | |
|---|---|
| Strong | ● |
| Moderate | ○ |
| Weak | ▽ |

| Direction of Improvement | |
|---|---|
| Maximize | ▲ |
| Target | ◇ |
| Minimize | ▼ |

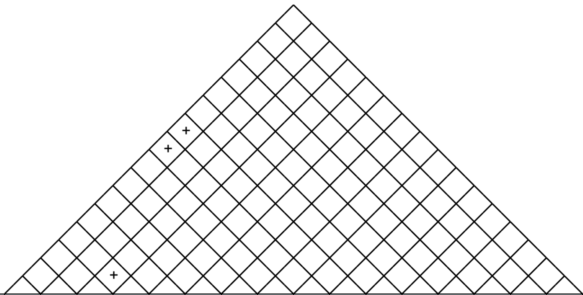


| Column # | 1 | 2 | 3 | 4 | 5 | 6 | 7 | 8 | 9 | 10 | 11 | 12 | 13 | 14 | 15 | 16 |
|---|---|---|---|---|---|---|---|---|---|---|---|---|---|---|---|---|
| Direction of Improvement | ▼ | ◇ | ▲ | ▲ | ▲ | ▲ | ◇ | ◇ | ◇ | ▲ | ◇ | ▼ | ▼ | | | |
| Functional Requirements | Price | Supplies MR-SAFE transducers | PRF | Max PRF with real time storing | ADC Resolution | Sampling Rate | External Trigger Input | GUI Interface | API / SDK | Number of Supported Transducers | USB Interface | Delivery Time | Size | | | |

| Row # | Weight Chart | Relative Weight | Customer Importance | Maximum Relationship | Customer Requirements (Explicit and Implicit) | 1 | 2 | 3 | 4 | 5 | 6 | 7 | 8 | 9 | 10 | 11 | 12 | 13 | 14 | 15 | 16 | Optel: Opbox 2.1 | Lecoeur electronique: US-EXPERT | US Ultratek: USB-UT350 | US Ultratek: USB-UT350M4 | Row # |
|---|---|---|---|---|---|---|---|---|---|---|---|---|---|---|---|---|---|---|---|---|---|---|---|---|---|---|
| 1 | | 12% | 8 | 9 | Cost | ● | | | | | | | | | | | | | | | | 5 | 3 | 1 | 1 | 1 |
| 2 | | 7% | 5 | 9 | Can supply MR-SAFE transducer | | ● | | | | | | | | | | | | | | | 5 | 0 | 0 | 0 | 2 |
| 3 | | 14% | 10 | 9 | Real-time sampling and storing | | | ○ | ● | | | | | | | | | | | | | 3 | 3 | 3 | 3 | 3 |
| 4 | | 14% | 10 | 9 | External source trigerring | | | | | | | ● | | | | | | | | | | 4 | 3 | 3 | 3 | 4 |
| 5 | | 12% | 8 | 3 | High resolution | | | | | ○ | ○ | | | | | | | | | | | 3 | 5 | 1 | 1 | 5 |
| 6 | | 12% | 8 | 9 | High sampling rate | | | | | | ● | | | | | | | | | | | 5 | 3 | 1 | 1 | 6 |
| 7 | | 10% | 7 | 9 | Ease-Of-Use | | | | | | | | ● | | | ○ | | ○ | | | | 4 | 4 | 4 | 4 | 7 |
| 8 | | 10% | 7 | 9 | Future Extendability | | | ▽ | ▽ | ▽ | ▽ | ○ | | ○ | ● | | | | | | | 3 | 3 | 3 | 5 | 8 |
| 9 | | 9% | 6 | 9 | Quick delivery | | | | | | | | | | | | ● | | | | | 4 | 4 | 1 | 1 | 9 |
| 10 | | | | | | | | | | | | | | | | | | | | | | | | | | 10 |
| 11 | | | | | | | | | | | | | | | | | | | | | | | | | | 11 |
| 12 | | | | | | | | | | | | | | | | | | | | | | | | | | 12 |
| 13 | | | | | | | | | | | | | | | | | | | | | | | | | | 13 |
| 14 | | | | | | | | | | | | | | | | | | | | | | | | | | 14 |
| 15 | | | | | | | | | | | | | | | | | | | | | | | | | | 15 |
| 16 | | | | | | | | | | | | | | | | | | | | | | | | | | 16 |

Customer Competitive Assesment

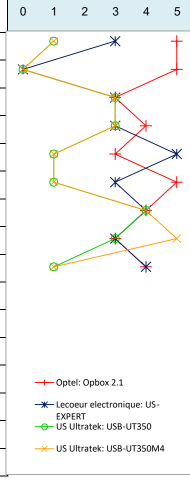


| | 1 | 2 | 3 | 4 | 5 | 6 | 7 | 8 | 9 | 10 | 11 | 12 | 13 | 14 | 15 | 16 |
|---|---|---|---|---|---|---|---|---|---|---|---|---|---|---|---|---|
| Target | As low as possible | Available | Minimum 100Hz | Minimum 100Hz | Minimum 8 bit | Mimimum 40 MSPS | Available, BNC connector preffered | Available | Available (as an option) | Mimumim 1 single element transducer | USB available (3.0 better than 2.0) | Max 2 weeks | As small as possible | | | |
| Max Relationship | 9 | 9 | 3 | 9 | 3 | 9 | 9 | 9 | 3 | 9 | 3 | 9 | 3 | | | |
| Technical Importance Rating | 104.35 | 65.217 | 53.623 | 140.58 | 44.928 | 149.28 | 160.87 | 91.304 | 30.435 | 91.304 | 30.435 | 78.261 | 30.435 | | | |
| Relative Weight | 10% | 6% | 5% | 13% | 4% | 14% | 15% | 9% | 3% | 9% | 3% | 7% | 3% | | | |
| Weight Chart | | | | | | | | | | | | | | | | |

Technical Competitive Assesment

| | 1 | 2 | 3 | 4 | 5 | 6 | 7 | 8 | 9 | 10 | 11 | 12 | 13 | 14 | 15 | 16 |
|---|---|---|---|---|---|---|---|---|---|---|---|---|---|---|---|---|
| Optel: Opbox 2.1 | 5 | 5 | 5 | 3 | 3 | 5 | 4 | 4 | 3 | 3 | 5 | 4 | 4 | | | |
| Lecoeur electronique: *US-EXPERT* | 4 | 0 | 5 | 3 | 5 | 3 | 3 | 4 | 5 | 3 | 5 | 4 | 4 | | | |
| US Ultratek: USB-UT350 | 3 | 0 | 5 | 3 | 1 | 1 | 3 | 4 | 3 | 3 | 5 | 2 | 4 | | | |
| US Ultratek: USB-UT350M4 | 2 | 0 | 5 | 3 | 1 | 1 | 3 | 4 | 3 | 5 | 5 | 2 | 4 | | | |

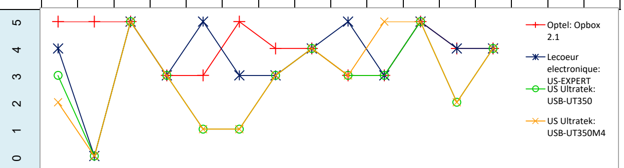


Column # | 1 | 2 | 3 | 4 | 5 | 6 | 7 | 8 | 9 | 10 | 11 | 12 | 13 | 14 | 15 | 16

Template Revision: 0.9 Date: 4/23/2010
Christopher Battles

# B RIG with De-hazing Results

## B.1 Histograms of performance metrics per activity on MR images with cartesian scanning trajectory

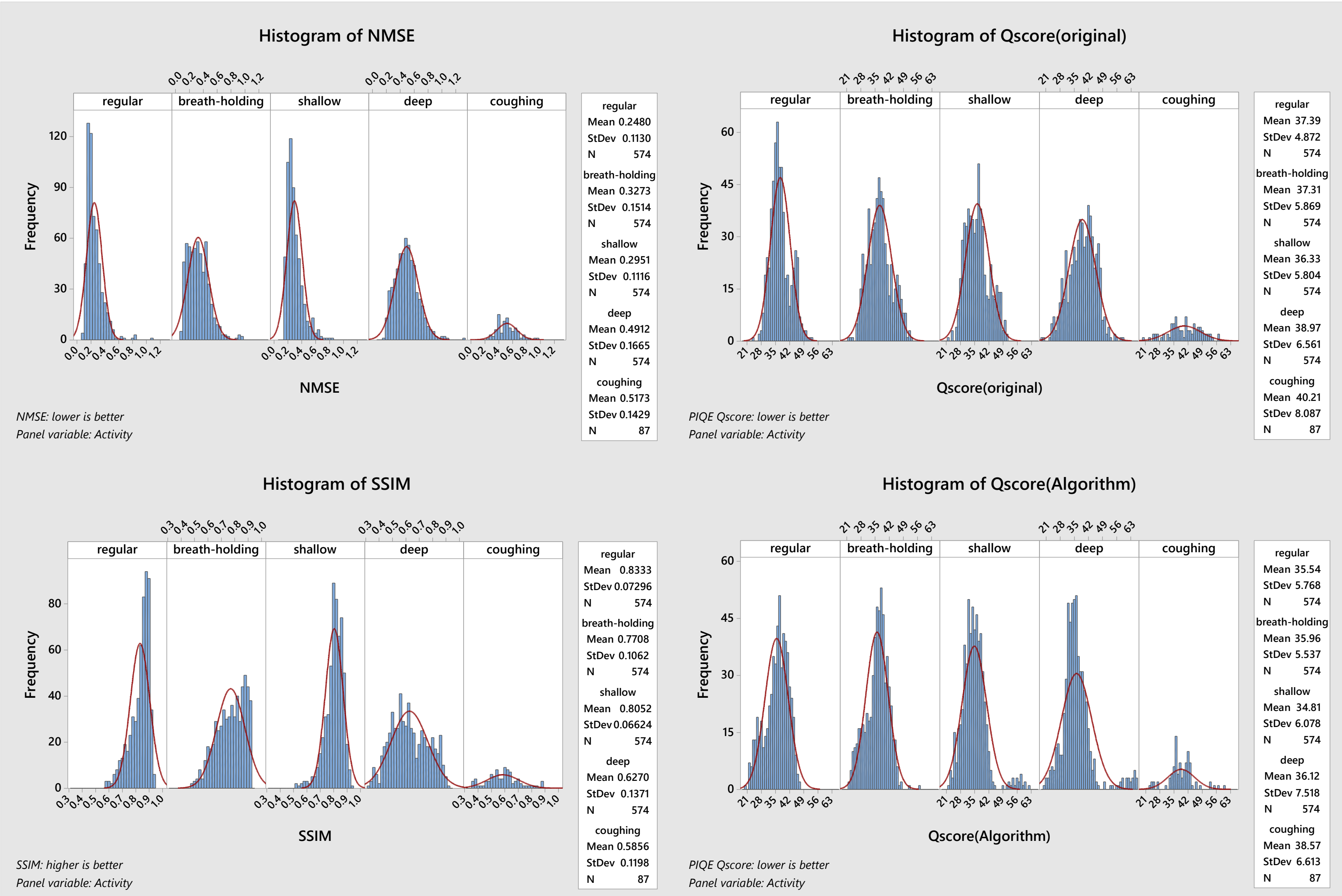

### B.2 Residual plots of performance metrics per activity on MR images with cartesian scanning trajectory

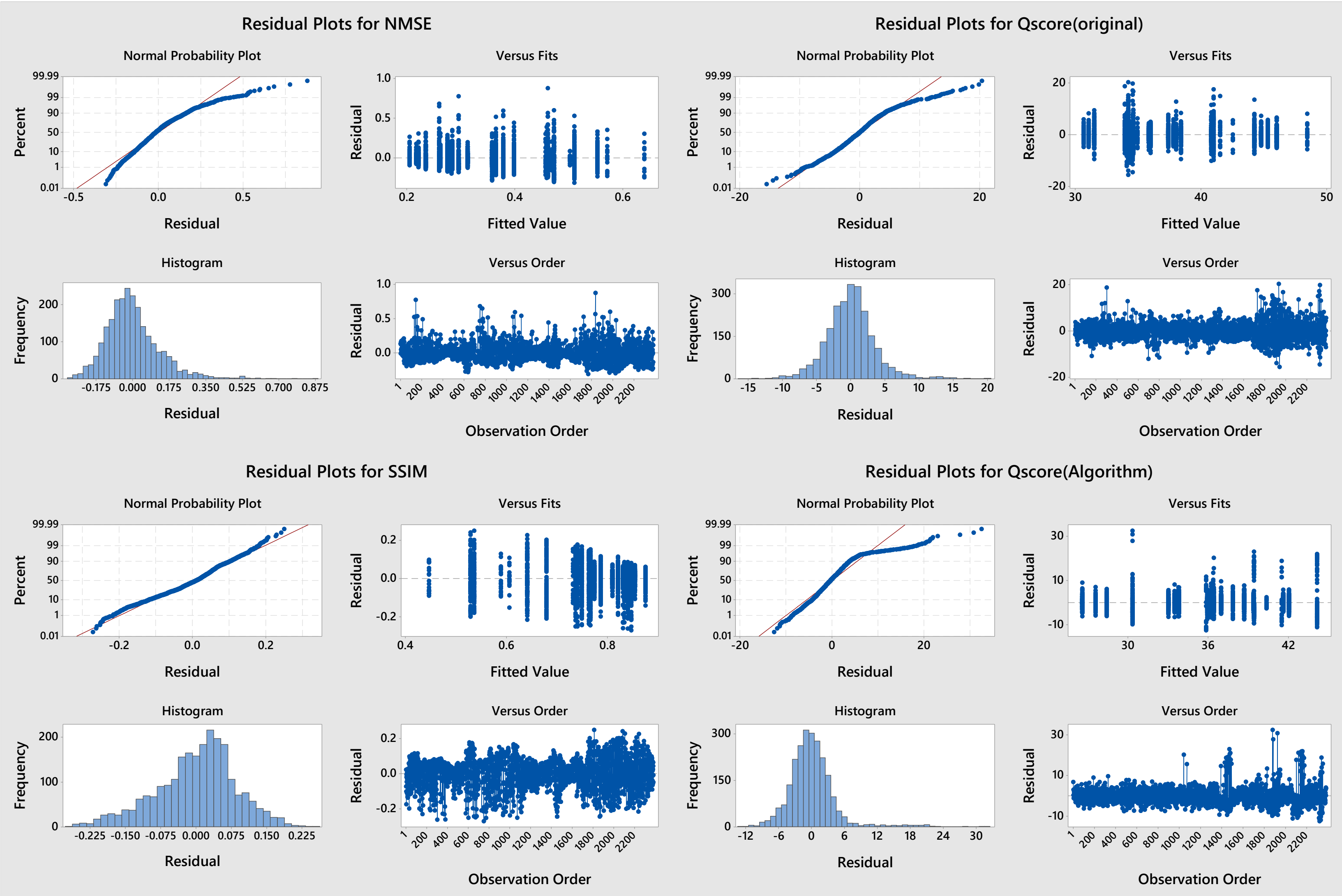

### B.3 Difference of means of performance metrics per activity on MR images with cartesian scanning trajectory

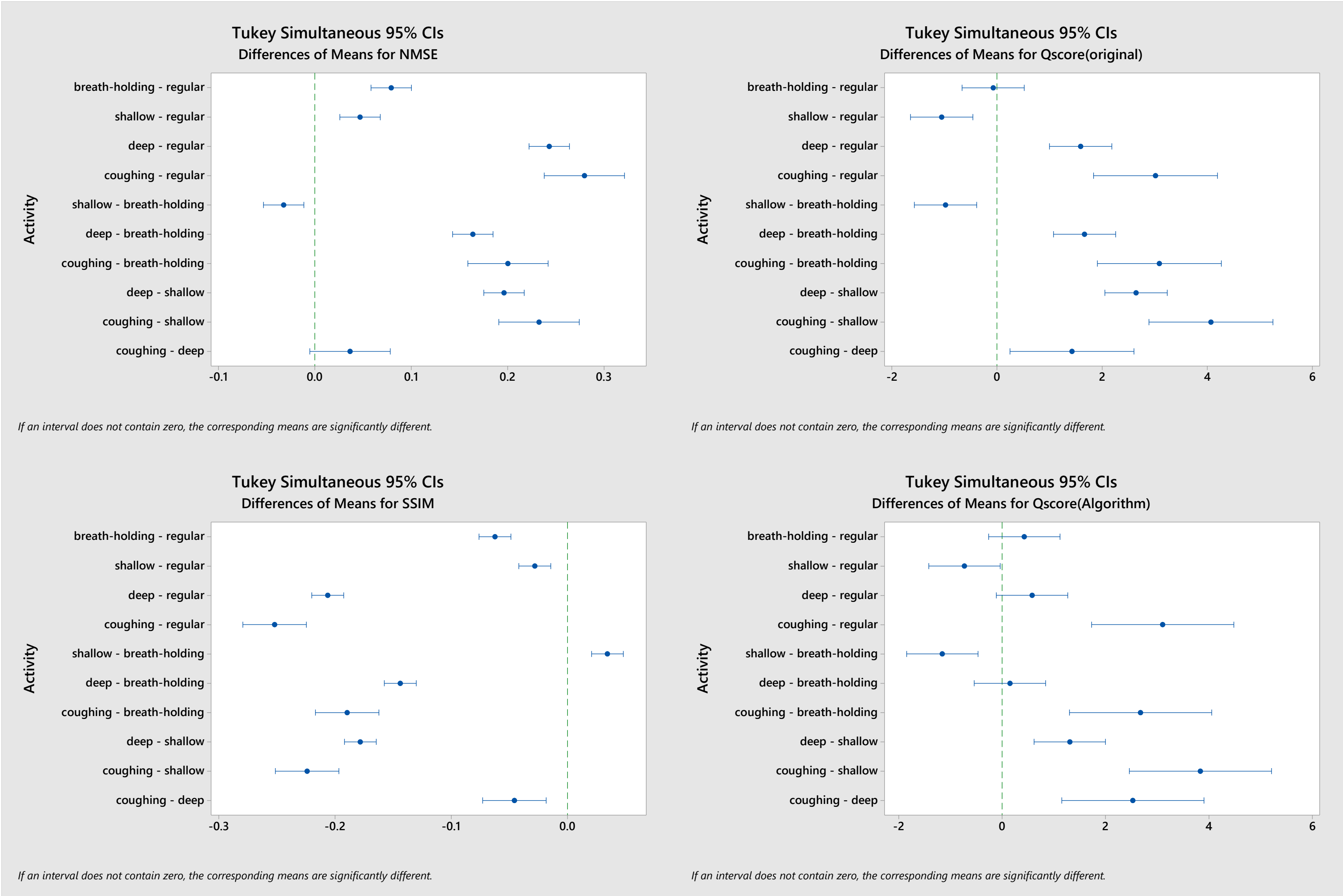

**B.4 Interval plot of Qscores on MR images generated with the cartesian scanning trajectory**

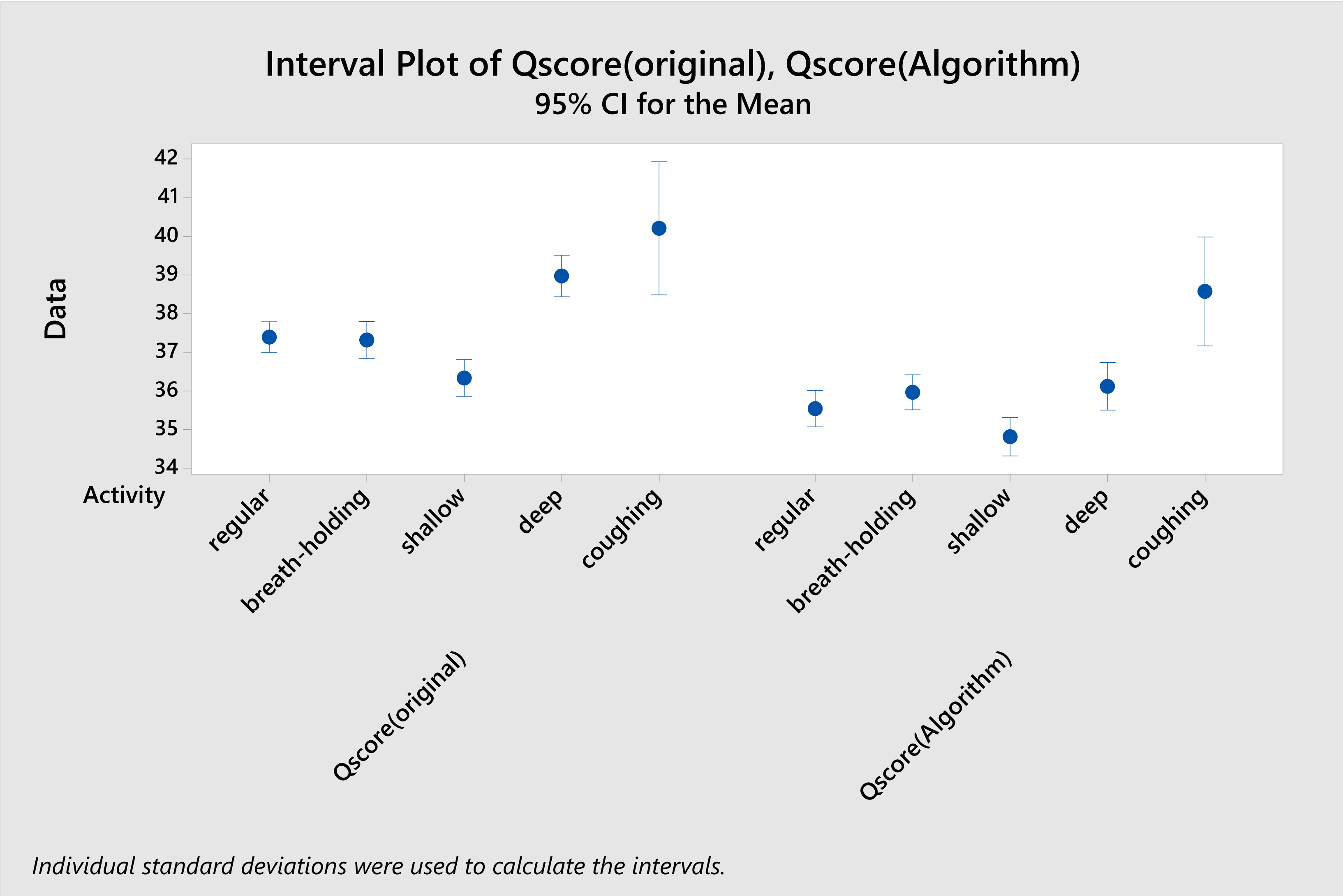

# C RKG with De-hazing Results

## C.1 Histograms of performance metrics per activity on MR images with cartesian scanning trajectory

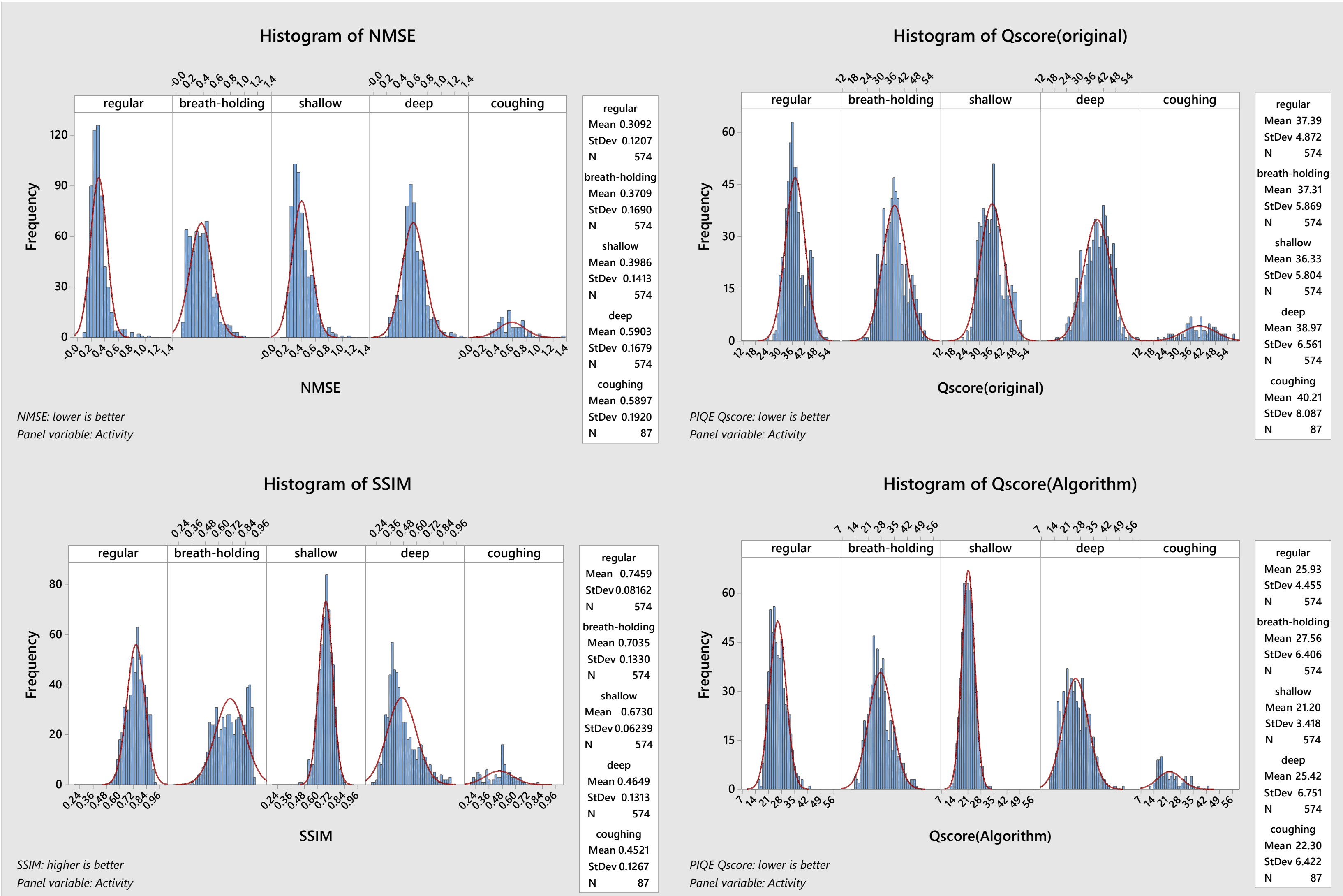

## C.2 Residual plots of performance metrics per activity on MR images with cartesian scanning trajectory

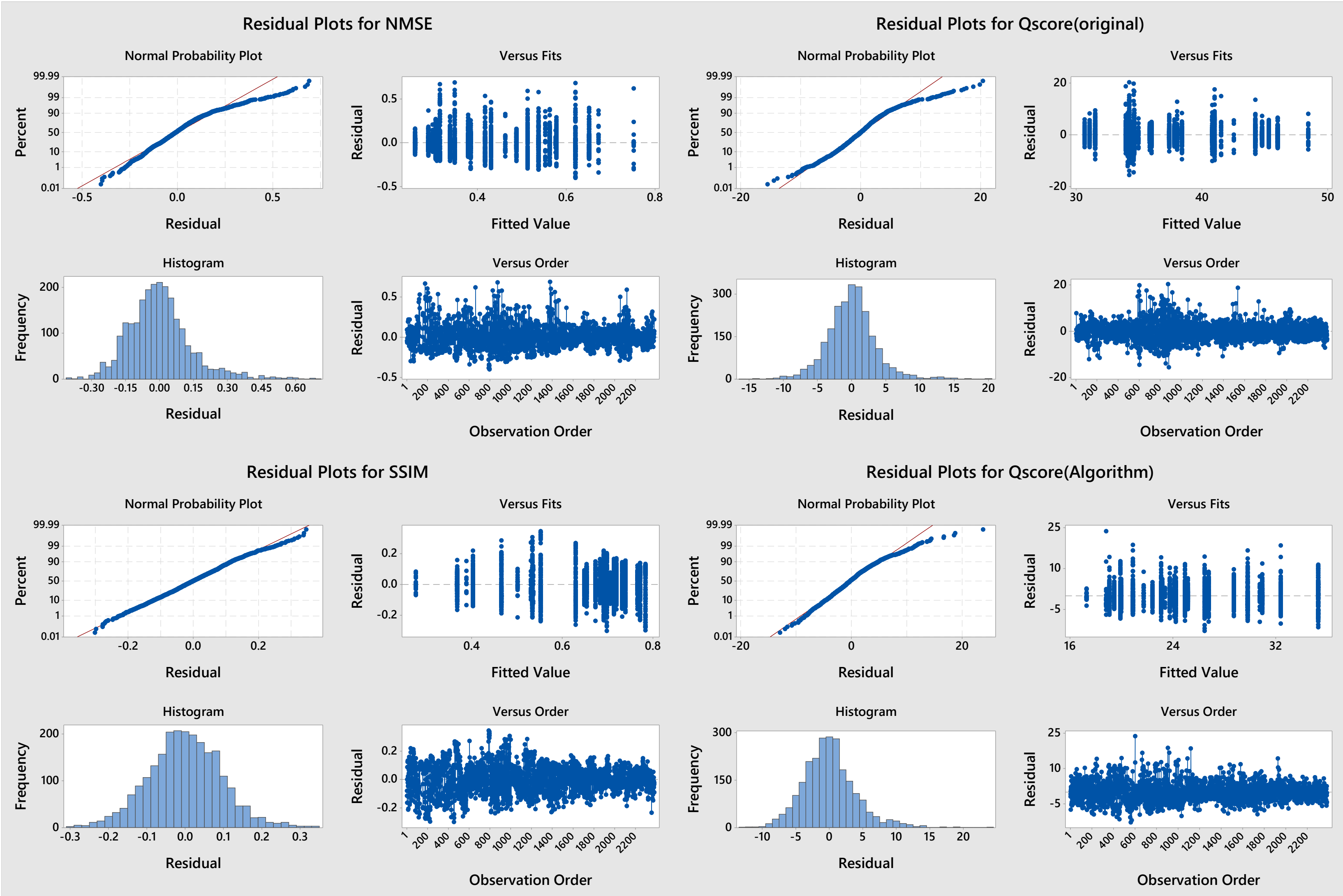

### C.3 Difference of means of performance metrics per activity on MR images with cartesian scanning trajectory

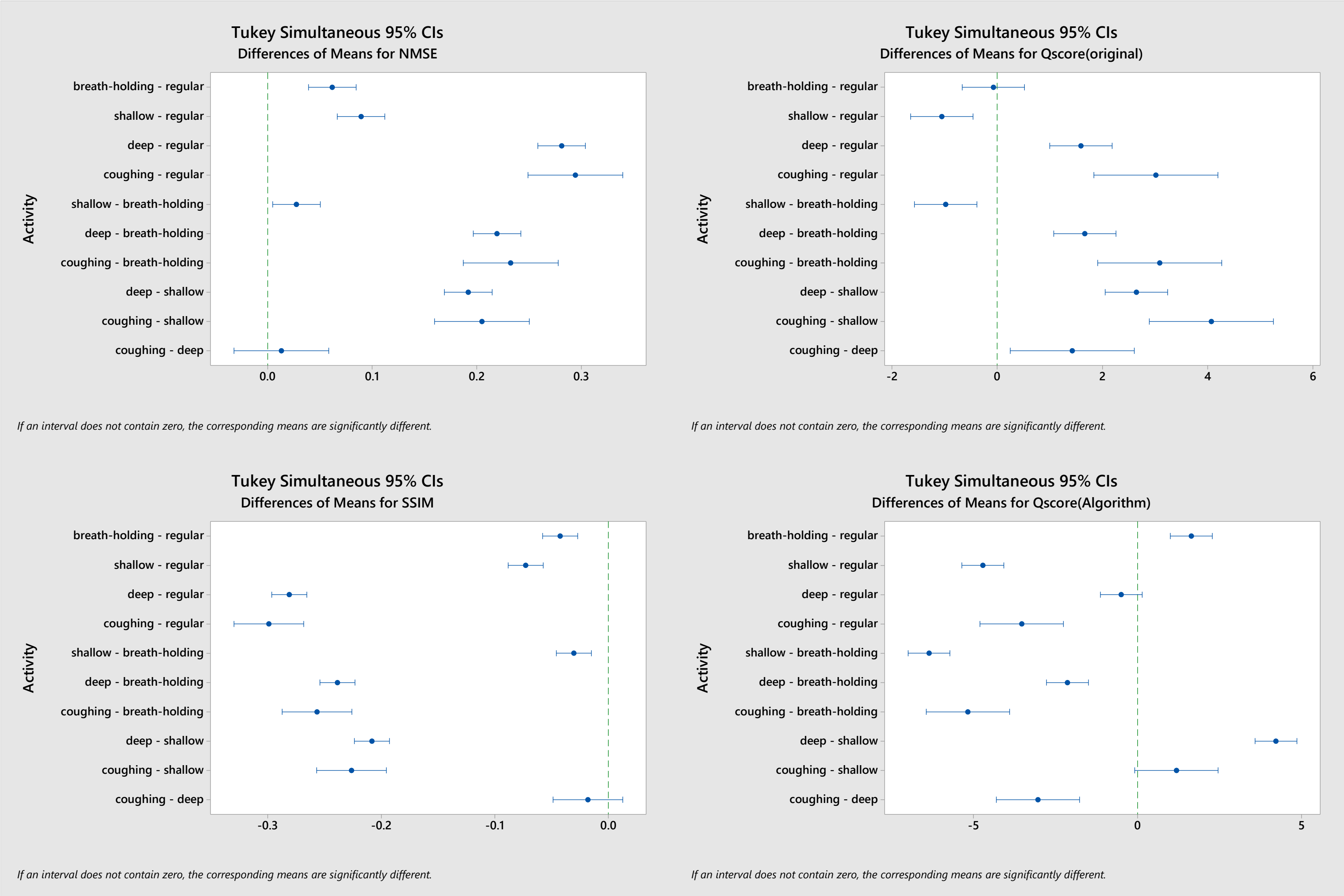

**C.4 Interval plot of Qscores on MR images generated with the cartesian scanning trajectory**

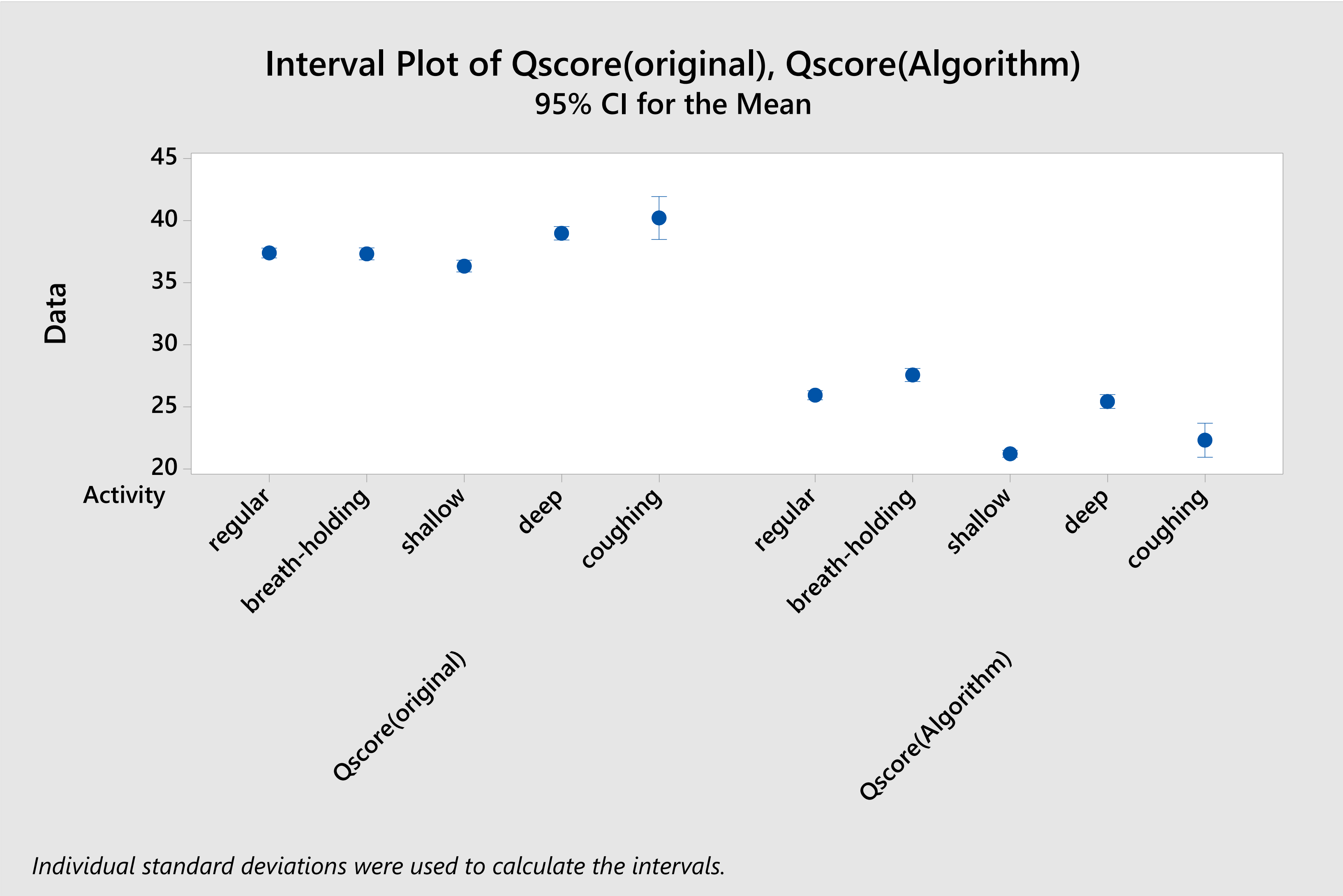

# D RIG Versus RKG

## D.1 Interval plot of the performance metrics per activity on MR images with cartesian scanning trajectory